

# Covariant Image Representation with Applications to Classification Problems in Medical Imaging

Dohyung Seo<sup>1</sup> · Jeffrey Ho<sup>1</sup> · Baba C. Vemuri<sup>1</sup>

Received: 8 October 2013 / Accepted: 22 June 2015 / Published online: 25 July 2015  
© Springer Science+Business Media New York 2015

**Abstract** Images are often considered as functions defined on the image domains, and as functions, their (intensity) values are usually considered to be invariant under the image domain transforms. This functional viewpoint is both influential and prevalent, and it provides the justification for comparing images using functional  $L^p$ -norms. However, with the advent of more advanced sensing technologies and data processing methods, the definition and the variety of images has been broadened considerably, and the long-cherished functional paradigm for images is becoming inadequate and insufficient. In this paper, we introduce the formal notion of covariant images and study two types of covariant images that are important in medical image analysis, symmetric positive-definite tensor fields and Gaussian mixture fields, images whose sample values covary i.e., jointly vary with image domain transforms rather than being invariant to them. We propose a novel similarity measure between a pair of covariant images considered as embedded shapes (manifolds) in the ambient space, a Cartesian product of the image and its sample-value domains. The similarity measure is based on matching the two embedded low-dimensional shapes, and both the extrinsic geometry of the ambient space and the intrinsic geometry of the shapes are incorporated in computing the similarity measure. Using

this similarity as an affinity measure in a supervised learning framework, we demonstrate its effectiveness on two challenging classification problems: classification of brain MR images based on patients' age and (Alzheimer's) disease status and seizure detection from high angular resolution diffusion magnetic resonance scans of rat brains.

**Keywords** Covariant images · Image graphs · Image matching · Image classification · Medical image applications

## 1 Introduction

This paper introduces the formal notion of covariant images and proposes a novel similarity measure  $S(\mathbf{X}, \mathbf{Y})$  for covariant images that has been shown experimentally to be effective for several classification problems arising from medical image analysis. Images are representations of discrete point samples of their underlying image functions on the image domain, and as such, they are often regarded as functions of the image domain. A characteristic feature of functions is the invariance of their sample values under image domain transforms, and this seemingly innocuous and often overlooked property provides the legitimacy to a large body of work on image matching and classification using  $L^2$  or other functional norms as the basic similarity measures between images. However, with more advanced sensing and signal processing technologies, images based on more powerful sampling methods and, consequently, more elaborate representations are becoming increasingly common, particularly in medical imaging applications. These images are often vector or tensor-valued and on occasions, they can even take values in a domain without vector-space structure. Notwithstanding this apparent diversity of sample-values, a common feature shared by these images is their general lack of con-

---

Communicated by M. Hebert.

✉ Baba C. Vemuri  
vemuri@cise.ufl.edu

Dohyung Seo  
dhseo@ufl.edu

Jeffrey Ho  
jho@cise.ufl.edu

<sup>1</sup> Department of Electrical and Computer Engineering,  
University of Florida, Gainesville, FL, USA

formity to the old functional paradigm of images in that their sample-values often change under image domain transforms. In other words, invariance of the sample-values gives way to the covariance<sup>1</sup> of the sample-values under image domain transforms, and an important but subtle consequence of the covariant image model is the greater degree of co-dependency between the image domain and sample-values as image domain transforms now affect the sample-values as well. Therefore, any principled approach for designing effective similarity measures for covariant images should take into account this implicit co-dependency between the image and sample-value domains that is the distinguishing feature of the covariant image model. Precisely because they lack incorporation of this co-dependency, similarity measures based on functional norms such as the  $L^2$ -distance measure lose much of their legitimacy in the new covariant context and for image classifications, their inadequacy and deficiency are often readily noticeable. The image similarity measure  $S(\mathbf{X}, \mathbf{Y})$  for covariant images proposed in this paper is intended to remedy the shortcomings of  $L^2$ -based functional norms in medical imaging applications, and the novel aspect of our approach is the central role played by the geometry in modeling the co-dependency between the image and sample-value domains.

A gray-scale or a color image contains samples of the radiance function of a scene, and each pixel's sample value records the flux of photons, essentially a directionless counting process. In contrast, the image functions sampled in medical image analysis are often more complex in nature in order to be biologically meaningful and clinically useful, and in particular, the image formation process often tries to capture directional quantities such as anisotropic diffusion along nerve fiber bundles in diffusion MR imaging. The qualitative difference between their respective image functions of interest explains much of the formal differences between processing images in medical image analysis and computer vision applications. In particular, image domain transforms that alter directions would naturally have nontrivial effect on directional quantities and hence on their sampling results, the sample-values. Although an exact modeling of the effect on sample-values is not possible, the first-order approximation assumes the change of sample-values depends on the local behavior of the transform. For smooth transforms, their local behaviors can be modeled by linear transforms, their Jaco-

bians, and the appearance of the Jacobians as local linear approximations allows us to formalize the notion of covariant images.

Specifically, a covariant image is formally given as a quintuple  $(\Omega, F, \mathcal{T}(F), \mathbf{I}, \mathcal{R})$ , where

- $\Omega$  is the image domain, taken to be the 2D or 3D unit square  $[0, 1]^k \subset \mathbb{R}^k$ ,  $k = 2$  or  $3$ .
- $F$  is the space of sample-values, and  $\mathcal{T}(F)$  is the set of smooth transformations of  $F$ .
- $\mathbf{I} : \Omega \rightarrow F$  is the image function, and to simplify notation, we will use  $\mathbf{I}$  to denote both the covariant image and its component image function.
- $\mathcal{R} : \mathbf{Mat}_k \rightarrow \mathcal{T}(F)$  is the re-orientation map with  $\mathbf{Mat}_k$  denoting the set of  $k \times k$  nonsingular matrices.

Since the image domain is a subset of  $\mathbb{R}^k$ , the Jacobian  $\mathbf{J}_{\mathbf{T}}(x)$  of a smooth transform  $\mathbf{T}$  at  $x \in \Omega$  can be represented as a  $k \times k$  nonsingular matrix. The map  $\mathcal{R}$  specifies exactly how the image  $\mathbf{I}$  transformed under an image domain transform  $\mathbf{T} \in \mathcal{T}(\Omega)$  according to the formula

$$\mathbf{T}_{\mathcal{R}}^*(\mathbf{I})(x) = \mathcal{R}(\mathbf{J}_{\mathbf{T}}(\mathbf{T}^{-1}x))(\mathbf{I}(\mathbf{T}^{-1}x)),$$

where  $\mathbf{T}_{\mathcal{R}}^*(\mathbf{I})$  denotes the transformed image, and on occasions, we will also denote it as  $(\mathbf{I} \circ \mathbf{T})_{\mathcal{R}}$ . We remark that  $\mathcal{R}$  is not assumed to be a homomorphism that preserves the algebraic structures between  $\mathbf{Mat}_k$  and  $\mathcal{T}(F)$ , and in applications,  $\mathcal{R}$  is typically given as a set of steps that produces the transform  $\mathcal{R}(\mathbf{J}_{\mathbf{T}}(\mathbf{T}^{-1}x))$  given the computed Jacobian  $\mathbf{J}_{\mathbf{T}}(\mathbf{T}^{-1}x)$ , a process that rarely makes  $\mathcal{R}$  a homomorphism. However, if  $\mathcal{R}$  is the trivial homomorphism mapping every element in  $\mathbf{Mat}_k$  to the identity transform in  $\mathcal{T}(F)$ , it then defines a special class of covariant images whose sample-values are not effected by the image domain transforms, the regular images. In this sense, the notion of covariant images strictly generalizes the usual notion of images, and it is the novel feature of the re-orientation map (when it is not trivial) that models the additional structure of co-dependency between spatial and sample-value domains. For a global linear transform  $\mathbf{T}$ , its Jacobian is a constant transform across  $\Omega$ , i.e., itself and therefore, the effect of  $\mathbf{T}$  on the sample-values is independent of  $x \in \Omega$ . However, for a general non-linear transform  $\mathbf{T}$ , its Jacobian is not a constant and its effect on the sample-values varies from point to point. In this paper, we study two classes of covariant images: symmetric positive-definite (SPD) tensor fields and Gaussian mixture fields. For the former, the space of sample-values  $F$  is the space of  $k \times k$  SPD matrices, and for the latter it is the space of Gaussian mixtures with a fixed number of components. Their respective details on re-orientation will be presented in the following sections.

<sup>1</sup> A word of caution here would serve in avoiding any confusion further down in the rest of this paper. In Computer Vision and Statistics, the term covariance is commonly used to indicate the second order statistic and should not be confused with the term we use here namely, "covariant". Further, in the field of tensor algebra, the terms, covariant and contravariant tensors are commonly used and indicate the way these tensors transform under coordinate transformations. In this paper, covariant images simply refers to images whose value set covaries or jointly varies with transformations applied to the domain.

Classification problems of interest in medical image analysis often require identifications of physiological or pathological features of some anatomical structures such as the ventricles, the corpus callosum, hippocampus etc. in the brain, and often times, some of the most useful and relevant features tend to be subtle variations in the shapes of these structures. Computationally, shape variations are usually characterized and quantified using image domain transforms and in particular, the magnitude of the transform that best matches two images often supplies an effective measure of similarity for a range of classification problems in medical imaging (e.g., Zhang et al. 2013). In the context of covariant images, a similarity measure  $\mathbf{S}(\mathbf{X}, \mathbf{Y})$  can be defined along the same line provided that an appropriate notion of matching for covariant images can be specified. The generalization process however is complicated by the re-orientation map  $\mathcal{R}$  that couples the hitherto incommensurable image and intensity domains, and to a lesser extent, the sample-value space  $F$  of greater generality. In particular, any appropriate matching formulation must demonstrate its compatibility with the re-orientation map  $\mathcal{R}$  that is the centerpiece of covariant images.

Mathematically, this requires the identification of the space in which the computation will take place and the metric with which the similarity can be measured. The re-orientation map  $\mathcal{R}$  makes it impossible to disentangle the sample-value domain  $F$  from the image domain  $\Omega$  as each domain by itself can not fully specify the action of  $\mathcal{R}$ . This naturally suggests their Cartesian product  $\Omega \times F$  as the candidate for the space in which the computations should take place. With  $\Omega \times F$ , a family of metrics can then be specified once a metric has been specified on  $\Omega$  and  $F$  separately. As a subset of  $\mathbb{R}^n$ , the metric for  $\Omega$  is easy to specify, and the difficulty is always with the metric selection for  $F$  since for a general sample-value space  $F$ , it is not clear what metric is appropriate. However, if  $\mathcal{R}$ -compatibility of the metric is interpreted as its invariance under re-orientation, then in many interesting cases, there exists only one such metric (up to an unimportant scaling) for  $F$ , settling the perennial thorny issue of metric selection. With the space and metric determined, the final component in defining  $\mathbf{S}(\mathbf{X}, \mathbf{Y})$  is to consider each image  $\mathbf{X}$  as an embedded shape (submanifold) in  $\Omega \times F$ , and to interpret image matching as shape matching in  $\Omega \times F$ . The similarity measure is based on matching the two embedded low-dimensional shapes, and both the extrinsic geometry of the ambient space and the intrinsic geometries of the shapes (images) are incorporated in computing the similarity measure: the point(pixel)-wise comparisons measured by the extrinsic geometry and the aggregation of the point-wise comparisons weighted by the intrinsic geometry. The matching process is formulated in a symmetric manner to ensure the symmetry of  $\mathbf{S}(\mathbf{X}, \mathbf{Y})$ . Compared with the  $L^p$ -norm, inputs from different geomet-

ric considerations permit greater improvements in specificity and flexibility as the intrinsic geometry furnishes an image-specific weighting scheme (essentially based on its edge structure) and the extrinsic geometry provides a flexible setting for incorporating additional features.

This paper provides the mathematical and computational details for realizing the slew of ideas described above. Specifically, we propose a novel similarity measure for covariant images based on matching two embedded image graphs as geometric shapes, with the emphasis on capturing the similarities/dissimilarities between two covariant images. In particular, we develop a geometric approach for matching general covariant images and present the mathematical details for the aforementioned two types of covariant images of importance in medical image analysis. The resulting optimization problem can be handled very efficiently since the major part of the gradient computation is achieved via useful analytical expressions. For validation tests, we show that the computed similarities can be used as the affinity measures in a supervised learning framework to yield competitive results on challenging classification problems in medical image analysis. Specifically, we report classification experiments that use a covariant image classification framework proposed in this paper for the classifications of brain MR images and high angular resolution diffusion magnetic resonance images, and experimental results show that the proposed approach is capable of producing impressive results for several interesting classification problems that include classifying the MR brain images of Alzheimer's disease patients and detecting seizures from (rat) brain images.

## 2 Related Work

Image registration is a well studied problem in medical image analysis. Registration requires defining a similarity measure,  $\mathbf{S}(\mathbf{X}, \mathbf{Y})$ , and needless to say that there is a large body of medical image analysis literature devoted to image registration. There are methods using landmarks, contours, surfaces or volumes [references in Christensen and Johnson (2001)]. The most popular metrics are mostly  $L^2$ -based metrics, and in image registration, both the data fidelity as well as the deformation regularization are often measured using  $L^2$ -metric (Christensen and Johnson 2003; Christensen et al. 1996; Joshi et al. 2004; Beg et al. 2005; Cao et al. 2006). Additionally, symmetric registration frameworks for various types of images have also been investigated in the literature (Christensen and Johnson 2001; Johnson and Christensen 2002; Christensen and Johnson 2003; Tagare et al. 2009; Cheng et al. 2009). While registration algorithms proposed in Christensen and Johnson (2001), Johnson and Christensen (2002), Christensen and Johnson (2003) are approximately symmetric, the exact symmetric formulation has been introduced

and studied in great depth in [Tagare et al. \(2009\)](#). In particular, an important point elucidated in [Tagare et al. \(2009\)](#) is the role played by the measure used to define the integral for computing the  $L^2$ -norm. While most earlier work simply settled for the standard Lebesgue measure  $\omega$  in  $\mathbb{R}^n$ , ([Cachier and Rey 2000](#)) followed by [Tagare et al. \(2009\)](#) proposed a transform-dependent measure to ensure symmetric registration, and for a transform  $\gamma$ , their novel measure is essentially a weighted Lebesgue measure  $(1 + J_\gamma)\omega$  with the weight determined by  $J_\gamma$ , the determinant of the Jacobian matrix of  $\gamma$ . Alternatively, a different method was introduced in [Cheng et al. \(2009\)](#) that also guarantees symmetric registration. Instead of tinkering with measures, their methods are relative in nature as the registration map is essentially factored through a third domain, the common domain. As its name suggest, the two images to be registered are transferred to the common domain for comparison, and the registration map is the product of the two transforms (or their inverses) that map the common domain to the two images. The factorization approach circumvents the symmetry issue, and it also has the added flexibility of handling simultaneous registration of multiple images.

Shape matching has also been studied quite extensively in the fields of computer graphics and computational geometry (e.g., [Litke et al. 2005](#)). However, most of these earlier works were invariably focused on shapes in low-dimensional Euclidean spaces such as  $\mathbb{R}^3$ , and for our intended applications that often require non-Euclidean ambient spaces, these earlier works are insufficient and inadequate. In particular, mathematical and computational details of our method are often more complicated and elaborate due to its non-Euclidean setting. Furthermore, issues such as symmetric registration that are important for medical image applications were seldom addressed by these earlier works which originated in different application domains. Additionally, parametric invariance is usually required for shape matching algorithms that operate on parametric shapes, and an important issue of re-parameterization in 2D closed surface matching has been investigated in [Kurtek et al. \(2010, 2011\)](#). This work introduced the idea of q-maps as a novel representation for shapes in order to solve the re-parameterization issue within the common  $L^2$ -based 3D shape matching framework. However, if the ambient space is non-Euclidean, it is not immediately clear how to extend the centering step in the construction of the q-map, and it does not appear at the moment that such an extension is straightforward or even possible.

Finally, image graphs have been used previously for anisotropic image smoothing, image enhancement and segmentation ([Sochen et al. 1998](#); [Kimmel and Sochen 1999](#); [Kimmel et al. 2000](#); [Gur and Sochen 2009](#); [Seo and Vemuri 2009](#)). In these works, image processing operations such as smoothing are often formulated as operations that directly

modify the geometry of the image graphs in order to achieve the desired results. However, images and hence their image graphs are always considered individually, and image graphs have not been used in problems that require considering more than one image. To the best of our knowledge, image graphs have not been used for matching images or computing their similarities in the way proposed here with the exception of [Cachier et al. \(2003\)](#) wherein, images are treated as point sets in 3D and the image matching problem is then posed as a point cloud matching problem which is solved using a variant of the iterated closest point (ICP) algorithm. Note that this approach does not take advantage of the underlying surface geometry of an image graph as is done in our work here. Despite the impressive results reported in these papers, Koenderink and van Doorn have argued against using image graphs (of RGB images) and their associated differential invariants in a provocatively-titled paper ([Koenderink and Doorn 2002](#)). Essentially, their argument is based on the incommensurability of the image and intensity domains, and in particular, notions such as image graphs that depend on blurring the distinction between the two domains have no theoretical foundations. Compared with RGB images, covariant images are not raw sampled signals that, for example, only count the impacting photons. Instead, they are representations of the signals that have often been processed beyond their initial raw stage, with the processing often involving image domain operations. Therefore, for covariant images, the two previously independent domains are now related through the re-orientation map  $\mathcal{R}$ , and this explicit “asymmetry breaking” between the image and intensity domains, so to speak, considerably lessens the importance of incommensurability. Hence, Koenderink and van Doorn’s viewpoint does not invalidate the use of image graphs for covariant images. It is interesting to note that the geometry model proposed in [Koenderink and Doorn \(2002\)](#) is based on an exotic family of transforms that relate the image and intensity domains. Although their context is different from ours, this nevertheless highlights, for image processing, the importance of identifying the correct group of transforms and elucidating their effects on the image domain and intensity values.

### 3 A Similarity Measure for Covariant Images

In this section we present the details for the similarity measure  $S(\mathbf{X}, \mathbf{Y})$  for covariant images and discuss its computational and mathematical components for general covariant images. The specializations of the general framework introduced in this section to two specific types of covariant images will be given in the next section. As image graphs play a central role in defining  $S(\mathbf{X}, \mathbf{Y})$ , we will start with a brief review of their geometry.

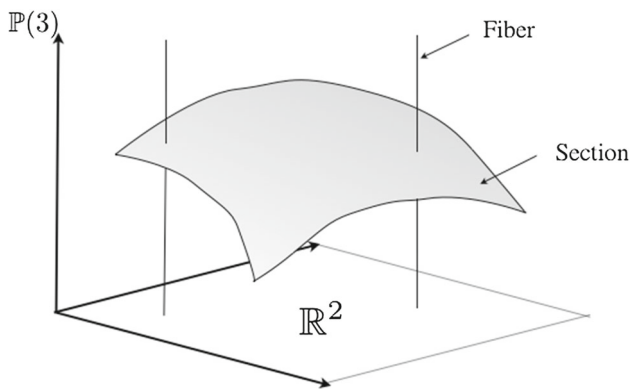


**Fig. 1** An illustration of a 3-by-3 symmetric positive-definite (SPD) tensor image in  $\mathbb{R}^3$  as a section of a fiber bundle. The total (ambient) space is  $E = \mathbb{R}^3 \times \mathbb{P}(3)$  (Gur and Sochen 2009)

### 3.1 Image Graphs

Among other applications, image graphs have been applied to anisotropic image smoothing (Kimmel and Sochen 1999; Kimmel et al. 2000; Gur and Sochen 2009), and Gur et al. provide a detailed review of the differential geometry of image graph (Gur and Sochen 2009). Specifically, an image is considered as a section of a trivial fiber bundle with projection map  $\pi E = \Omega \times F \xrightarrow{\pi} \Omega$  (Gur and Sochen 2009; Koenenderink and Doorn 2002) where  $\Omega$  (image domain) and  $F$  (intensity i.e., sample-value domain) are the base manifold and the fiber, respectively, and  $E$  as the Cartesian product of the base manifold and fiber is the total space. Recall that a section of the fiber bundle is a mapping  $\mathbf{X} : \Omega \rightarrow E$  such that the composition  $\pi \circ \mathbf{X}$  is the identity on  $\Omega$ , and Fig. 1 shows a 3-by-3 SPD tensor image as a section of a fiber bundle whose total space is  $E = \mathbb{R}^3 \times \mathbb{P}(3)$ . Geometrically, the image graph is the subset of  $E$  defined by the image of the section  $f$ , and in practice, the image graph is then considered as an embedded submanifold in the ambient space  $E$ .

The differential geometry of the image graph is specified by its Riemannian metric tensor and for our purpose, the main interest is on the Riemannian volume form that would allow us to integrate over the image graph. The general formulas for computing the metric tensor and volume form are well-known (DoCarmo 1992), and specializing to images defined on  $\Omega \subset \mathbb{R}^3$ , we have the following. Let  $\mathbf{X}$  denote both the covariant image and its corresponding section,

$$\mathbf{X} : (x, y, z) \rightarrow (\mathbf{r}, \mathbf{I}(\mathbf{r})), \tag{1}$$

where  $\mathbf{r} = (x, y, z)$  and  $\mathbf{I}$  is the intensity value of  $\mathbf{X}$  at  $(x, y, z) \in \Omega$ . Computationally, the section map  $\mathbf{X}$  serves as a global parameterization of the image graph using  $\Omega \subset \mathbb{R}^3$  as its parameter domain, and all local geometric quantities of interest are phrased in terms of the derivatives of  $\mathbf{X}$  with

respect to the three coordinates  $x, y, z$ . We first equip the total space  $E = \Omega \times F$  with the product Riemannian metric  $\mathbf{G}$  that is the product of the Euclidean metric on  $\mathbb{R}^3$  and a metric  $\mathbf{H}$  for the fiber  $F$ . The product Riemannian metric specifies a non-degenerate bilinear form  $\langle \mathbf{u}, \mathbf{v} \rangle_{\mathbf{G}}$  for tangent vectors at each point in  $E$ , and  $\langle \mathbf{u}, \mathbf{v} \rangle_{\mathbf{G}}$  can be represented by a block-diagonal matrix that clearly indicates its product structure ( $\mathbf{H}$  is the fiber metric)

$$\mathbf{G} = \begin{pmatrix} \lambda & 0 & 0 & 0 \\ 0 & \lambda & 0 & 0 \\ 0 & 0 & \lambda & 0 \\ 0 & 0 & 0 & \mathbf{H} \end{pmatrix}. \tag{2}$$

Using the product metric  $\mathbf{G}$ , the Riemannian metric tensor of the image graph is given by

$$\mathbf{K} = \begin{pmatrix} \langle \mathbf{X}_u, \mathbf{X}_u \rangle_{\mathbf{G}} & \langle \mathbf{X}_u, \mathbf{X}_v \rangle_{\mathbf{G}} & \langle \mathbf{X}_u, \mathbf{X}_w \rangle_{\mathbf{G}} \\ \langle \mathbf{X}_v, \mathbf{X}_u \rangle_{\mathbf{G}} & \langle \mathbf{X}_v, \mathbf{X}_v \rangle_{\mathbf{G}} & \langle \mathbf{X}_v, \mathbf{X}_w \rangle_{\mathbf{G}} \\ \langle \mathbf{X}_w, \mathbf{X}_u \rangle_{\mathbf{G}} & \langle \mathbf{X}_w, \mathbf{X}_v \rangle_{\mathbf{G}} & \langle \mathbf{X}_w, \mathbf{X}_w \rangle_{\mathbf{G}} \end{pmatrix}, \tag{3}$$

where  $\mathbf{X}_u, \mathbf{X}_v, \mathbf{X}_w$  are the partial derivatives of  $\mathbf{X}$  with respect to  $u, v, w$ , respectively, considered as tangent vectors in  $E$ . The Riemannian volume  $d\omega$  form follows immediately from the metric tensor according to the formula

$$d\omega = \sqrt{\kappa} \, dudvdw, \tag{4}$$

where  $\kappa$  is the determinant of  $\mathbf{K}$ .

### 3.2 Similarity Measure $S(\mathbf{X}_1, \mathbf{X}_2)$

Given the image domain  $\Omega$ , we denote  $\mathbf{T}(\Omega)$  the set of transforms in  $\Omega$ , smooth bijective transforms that fix the boundary of  $\Omega$ . A transform  $\Psi$  in  $\mathbf{T}(\Omega)$  is then represented by its deformation field  $(U, V, W)$  on  $\Omega$ :

$$\begin{pmatrix} u_2 \\ v_2 \\ w_2 \end{pmatrix} = \begin{pmatrix} u_1 + U(u_1, v_1, w_1) \\ v_1 + V(u_1, v_1, w_1) \\ w_1 + W(u_1, v_1, w_1) \end{pmatrix}, \tag{5}$$

With this representation, the magnitude of  $\Psi$  is measured by the squared-norm of its displacement field:

$$\|\Psi\|_{\Omega}^2 = \int_{\Omega} (|U|^2 + |V|^2 + |W|^2) d\Omega. \tag{6}$$

In addition, the Jacobian of  $\Psi$  is then conveniently given by

$$\mathbf{J}_{\Psi} = \begin{pmatrix} 1 + U_{u_1} & U_{v_1} & U_{w_1} \\ V_{u_1} & 1 + V_{v_1} & V_{w_1} \\ W_{u_1} & W_{v_1} & 1 + W_{w_1} \end{pmatrix}, \tag{7}$$

where the subscripts denote the variables with respect to which the partial derivatives are taken. Let  $\mathbf{X}_1, \mathbf{X}_2$  denote two covariant images with their image graph representations

$$\begin{aligned} \mathbf{X}_1 &: (u_1, v_1, w_1) \rightarrow (\mathbf{r}_1, \mathbf{I}_1(\mathbf{r}_1)) \\ \mathbf{X}_2 &: (u_2, v_2, w_2) \rightarrow (\mathbf{r}_2, \mathbf{I}_2(\mathbf{r}_2)), \end{aligned} \tag{8}$$

with  $\Omega$  the image domain. Comparison of these two image graphs is based on the product metric in  $E$  that gives the squared distance  $\mathbf{Dist}^2(\mathbf{e}_1, \mathbf{e}_2)$  between two points  $\mathbf{e}_1 = (u_1, v_1, w_1, \mathbf{I}_1), \mathbf{e}_2 = (u_2, v_2, w_2, \mathbf{I}_2) \in E$  as

$$\lambda((u_1 - u_2)^2 + (v_1 - v_2)^2 + (w_1 - w_2)^2) + \mathbf{Dist}_F^2(\mathbf{I}_1, \mathbf{I}_2), \tag{9}$$

where  $\mathbf{Dist}_F^2(\mathbf{I}_1, \mathbf{I}_2)$  is the squared-distance between the two points  $\mathbf{I}_1, \mathbf{I}_2$  in the fiber  $F$  using the fiber metric.

Intuitively, the similarity measure  $\mathbf{S}(\mathbf{X}_1, \mathbf{X}_2)$  between two covariant images  $\mathbf{X}_1, \mathbf{X}_2$  is defined as the magnitude of the image domain transform  $\Psi$  that best matches the two image graphs as shapes in the total space  $E$ . This is made precise by defining  $\mathbf{S}(\mathbf{X}_1, \mathbf{X}_2)$  as

$$\mathbf{S}(\mathbf{X}_1, \mathbf{X}_2) = \|\Psi\|_{\Omega}^2,$$

where  $\Psi$  is the minimum of a two-term objective function that is the sum of the matching cost and regularization (with  $L_r > 0$ ):

$$\begin{aligned} \Psi &= \arg \min_{\gamma \in \mathbf{T}(\Omega)} \mathbf{E}(\gamma; \mathbf{X}_1, \mathbf{X}_2) \\ &= \arg \min_{\gamma \in \mathbf{T}(\Omega)} \mathbf{E}_m(\gamma; \mathbf{X}_1, \mathbf{X}_2) + L_r \mathbf{E}_r(\gamma). \end{aligned}$$

The matching cost function  $\mathbf{E}_m(\gamma; \mathbf{X}_1, \mathbf{X}_2)$  is a function of the transform  $\gamma$ , and each  $\gamma$  provides a particular correspondence between points on  $\mathbf{X}_1$  and  $\mathbf{X}_2$ . The distance between a pair of corresponding points is measured by the metric in  $E$  and for each  $\gamma$ ,  $\mathbf{E}_m(\gamma; \mathbf{X}_1, \mathbf{X}_2)$  integrates these point-wise distances over the image graphs using their Riemannian volume forms, giving a cost function that can easily be shown to be symmetric:

$$\mathbf{E}_m(\gamma) = \int \mathbf{Dist}^2(\mathbf{X}_1, \mathbf{X}_2 \circ \gamma) (\sqrt{\kappa_1} + \sqrt{\kappa_2(\Omega_2 \circ \gamma)}) J_\gamma d\Omega_1$$

where  $J_\gamma$  the determinant of the Jacobian,  $\mathbf{J}_\gamma$  and  $\sqrt{\kappa_1} d\Omega_1$  and  $\sqrt{\kappa_2} d\Omega_2$  denote the Riemannian volume forms on  $\mathbf{X}_1, \mathbf{X}_2$ , respectively (Fig. 2). If  $(U, V, W)$  is the displacement field of  $\gamma$ ,  $\mathbf{Dist}^2(\mathbf{X}_1, \mathbf{X}_2 \circ \gamma)$  can be given more precisely as (following Eq. 9)

$$\mathbf{Dist}^2(\mathbf{X}_1, \mathbf{X}_2 \circ \gamma) = \lambda(U^2 + V^2 + W^2) + \mathbf{Dist}_F^2(\mathbf{I}_1, \mathbf{I}_2 \circ \gamma), \tag{10}$$

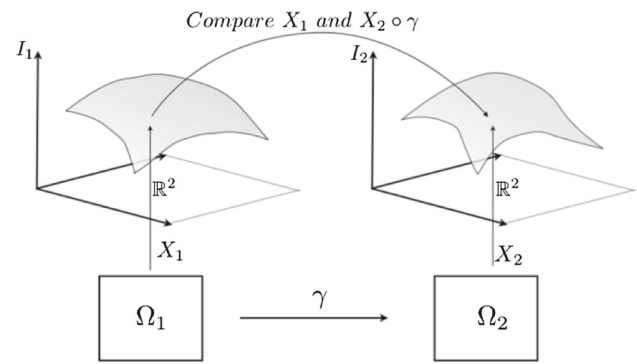


**Fig. 2** Matching images as image graphs can be realized via registration map  $\gamma$  defined between the two surfaces. The two surfaces represent 2D image graphs or 2D slices of 3D image graphs

The regularization term  $\mathbf{E}_r(\gamma)$  is the standard symmetric regularization scheme using the Jacobian field  $\mathbf{J}_\gamma$  as proposed in [Tagare et al. \(2009\)](#), [Yanovsky et al. \(2007\)](#)

$$\mathbf{E}_r(\gamma) = \int (J_\gamma - 1) \log(J_\gamma) d\Omega_1. \tag{11}$$

In our framework, we do not adopt a diffeomorphic approach such as LDDMM or its variants. Therefore, our regularization term may not be able to guarantee diffeomorphisms. However, the regularization in our work requires the determinant of Jacobian to be close to one and/or positive which is a necessary condition for diffeomorphisms. However, if the smoothness coefficient is not large enough, this requirement is violated. At each registration, we check for the positivity of the determinant of Jacobian. If there are set of pixels/voxels where the determinants are negative, we tune the penalty constraint by an appropriate amount to satisfy this constraint.

*Remark* In the two-term objective function,  $\mathbf{E}(\gamma; \mathbf{X}_1, \mathbf{X}_2)$ , the geometries of the covariant images  $\mathbf{X}_1, \mathbf{X}_2$  are incorporated in the first term  $\mathbf{E}_m(\gamma; \mathbf{X}_1, \mathbf{X}_2)$ . In its integral definition, the integrand  $\mathbf{Dist}^2(\mathbf{X}_1, \mathbf{X}_2 \circ \gamma)$  depends on the extrinsic geometry since it uses the distance of the ambient space  $E$ . On the other hand, the integral measure,  $(\sqrt{\kappa_1} + \sqrt{\kappa_2(\Omega_2 \circ \gamma)}) \mathbf{J}_\gamma d\Omega_1$  comes entirely from the intrinsic geometries of  $\mathbf{X}_1, \mathbf{X}_2$  that furnish the volume forms  $\kappa_1, \kappa_2$ , respectively. In particular, from Eq. 3, it follows that the forms  $\kappa_1, \kappa_2$  are products of various derivatives of  $\mathbf{I}_1$  and  $\mathbf{I}_2$ , respectively, and for points near or on an edge, relatively large magnitudes of their derivatives generally correspond to larger values for  $\kappa_1$  and  $\kappa_2$ . Consequently, the integral provides greater weights to regions near or on an edge,<sup>2</sup> and for a similarity measure that is designed to pick up subtle variations in shape, this is a desirable feature, a direct consequence of the pure geometric formulation.

<sup>2</sup> A similar observation is also made in [Sochen et al. \(1998\)](#).

### 3.3 Computational Details and Optimization

To effectively determine the matching transform  $\Psi$  as the minimum of the objective function  $\mathbf{E}(\gamma; \mathbf{X}_1, \mathbf{X}_2)$ , it is necessary to work with a computationally useful and efficient parameterization of  $\mathbf{T}(\Omega)$ . As it stands,  $\mathbf{T}(\Omega)$  is an infinite-dimensional nonlinear space and its exact parameterization is in general difficult. Instead, we will take advantage of the fact that computations will take place on a regular grid in  $\mathbb{R}^3$  and the representation of  $\Psi$  given in Eq. 5 naturally suggests expanding the components of the displacement field  $(U, V, W)$  using the orthogonal discrete sine and cosine (DSC) basis as was done in earlier work by Ashburner and Friston (1999). Specifically, the expansions of  $U, V, W$  are given by

$$\begin{aligned}
 U(u, v, w) &= \sum_{n=1, m, l=0} \mathcal{A}_{nml} \Phi_{U_{nml}}(u, v, w) \\
 V(u, v, w) &= \sum_{m=1, n, l=0} \mathcal{B}_{nml} \Phi_{V_{nml}}(u, v, w) \\
 W(u, v, w) &= \sum_{l=1, n, m=0} \mathcal{C}_{nml} \Phi_{W_{nml}}(u, v, w)
 \end{aligned}$$

with the basis functions given by

$$\begin{cases}
 \Phi_{U_{nml}} = \mathcal{N}_u \sin(\mathcal{P}_{nh}(u)) \cos(\mathcal{Q}_{mw}(v)) \cos(\mathcal{Q}_{ld}(w)) \\
 \Phi_{V_{nml}} = \mathcal{N}_v \cos(\mathcal{Q}_{nh}(u)) \sin(\mathcal{P}_{mw}(v)) \cos(\mathcal{Q}_{ld}(w)) \\
 \Phi_{W_{nml}} = \mathcal{N}_w \cos(\mathcal{Q}_{nh}(u)) \cos(\mathcal{Q}_{mw}(v)) \sin(\mathcal{P}_{ld}(w))
 \end{cases} \tag{12}$$

where  $\mathcal{N}_{\{u,v,w\}}$  are normalization constants. The angular functions  $\mathcal{P}_{ab}(x), \mathcal{Q}_{ab}(x)$  are determined by the grid size  $\{h, w, d\} \in \mathbb{Z}^3$  such that  $u \in [0, h - 1], v \in [0, w - 1]$  and  $w \in [0, d - 1]$  and

$$\begin{aligned}
 \mathcal{P}_{ab}(x) &= \frac{\pi ax}{b - 1}, \\
 \mathcal{Q}_{ab}(x) &= \frac{\pi a(2x + 1)}{2b}.
 \end{aligned}$$

The coefficients  $\mathcal{A}_{nml}, \mathcal{B}_{nml}$  and  $\mathcal{C}_{nml}$  provide a linear parameterization of deformation fields on  $\Omega$ . While computationally convenient, this linear parameterization fails to guarantee the parameterized transforms are indeed bijective, although the degree of their smoothness can always be controlled by the coefficients. Furthermore, due to the sine functions in Eq. 12, deformations across the domain boundary are prevented.

While the objective function  $\mathbf{E}(\gamma; \mathbf{X}_1, \mathbf{X}_2)$  can now be considered as a function of  $\mathcal{A}_{nml}, \mathcal{B}_{nml}$  and  $\mathcal{C}_{nml}$ , its minimization is still quite challenging and often times, extra steps are required in order to bolster convergence or ensure the quality of the result. For example, in order to prevent

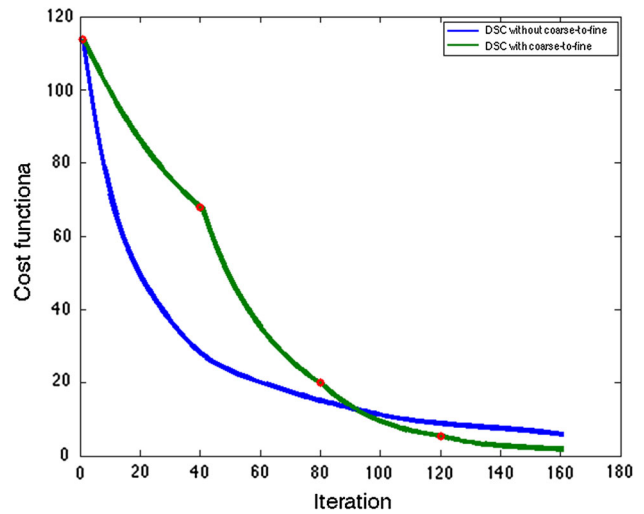


**Fig. 3** Plot of the values of the cost functional versus the number of iterations. The number of basis functions is increased after a fixed number of iterations, starting from the lowest frequency mode. The green/blue lines represents method with/without the coarse-to-fine strategy respectively. The points where additional high-frequency modes were introduced are marked red. Given a fixed number of iterations, computation speed with the coarse-to-fine (green line) is 1.5 times faster than the one without the coarse-to-fine (blue line) strategy (Color figure online)

entrapment at a local minimum in the early stage of the optimization, the coarse-to-fine grain method is often required. However, successive image down-sampling and up-sampling in coarse-to-fine grain approach can be undesirable on occasions. The DSC basis approach outlined above enables us to bypass this step, and instead of down-sampling images, it initiates the optimization with a small number of low-frequency components in the DSC basis expansion. High-frequency components are then successively introduced to further improve upon the current solution. Figure 3 displays the typical behavior of the value of the objective function during the optimization process with its characteristic pattern of diminishing value occurring in stages. We have compared the convergence pattern with/without of the coarse-to-fine strategy which are depicted in green/blue respectively. The plot shows that the overall convergence rate without the coarse-to-fine strategy is slower than the one with the coarse-to-fine strategy w.r.t. the number of iterations. In addition, Given same number of iterations, the compute time of the method with the coarse-to-fine strategy is 1.5 times faster than the one without the strategy in this test. The timing comparison was carried on an Intel Xenon 5520 CPU with Matlab GPU package for DSC computation with NVIDIA GTX 470.

The specific optimization method used is based on the nonlinear conjugate gradient (NCG) and the numerical algorithm for the optimization is outlined in Algorithm 1. An important ingredient in NCG is the evaluation of the gradient of the objective function, and while the objective function  $\mathbf{E}(\gamma; \mathbf{X}_1, \mathbf{X}_2)$  in general is too complicated to allow one sin-

gle closed-form formula for its gradient, we show below that its gradient can nevertheless be efficiently computed using a series of formulas that can be easily managed during computation.

The gradient vector is determined by the first-order partial derivatives of  $\mathbf{E}(\gamma; \mathbf{X}_1, \mathbf{X}_2)$  with respect to  $\mathcal{A}_{nml}$ ,  $\mathcal{B}_{nml}$  and  $\mathcal{C}_{nml}$ . It suffices to present only the derivation for  $\mathcal{A}_{nml}$  as the derivations for  $\mathcal{B}_{nml}$  and  $\mathcal{C}_{nml}$  follow suit. As  $\mathbf{E}(\gamma; \mathbf{X}_1, \mathbf{X}_2)$  is a sum of two terms, we have

$$\begin{aligned} & \frac{\partial}{\partial \mathcal{A}_{nml}} \mathbf{E}(\gamma, \mathbf{X}_1, \mathbf{X}_2) \\ &= \frac{\partial}{\partial \mathcal{A}_{nml}} \mathbf{E}_m(\gamma; \mathbf{X}_1, \mathbf{X}_2) + \frac{\partial}{\partial \mathcal{A}_{nml}} \mathbf{E}_r(\gamma). \end{aligned} \tag{13}$$

and from Eq. 13, there are three terms of interest namely,

$$\frac{\partial}{\partial \mathcal{A}_{nml}} \text{Dist}^2(\mathbf{X}_1, \mathbf{X}_2 \circ \gamma) \mathcal{R}, \tag{14}$$

$$\frac{\partial}{\partial \mathcal{A}_{nml}} \sqrt{\kappa_2(\Omega_2 \circ \gamma)} J_\gamma, \tag{15}$$

$$\frac{\partial}{\partial \mathcal{A}_{nml}} (J_\gamma - 1) \log(J_\gamma). \tag{16}$$

Equations 15 and 16 do not involve the sample values and re-orientation; they are the same for all covariant images regardless their type of sample values. The derivations for Eqs. 15 and 16 are provided in Appendix 2. With re-orientation, Eq. 14 can be rewritten as

$$\begin{aligned} & \frac{\partial}{\partial \mathcal{A}_{nml}} \text{Dist}^2(\mathbf{X}_1, \mathbf{X}_2 \circ \gamma) \mathcal{R} \\ &= 2\lambda U \Phi_{U_{nml}} + \frac{\partial}{\partial \mathcal{A}_{nml}} \text{Dist}_F^2(I_1, I_2 \circ \gamma) \mathcal{R}. \end{aligned} \tag{17}$$

The first term on the RHS is straightforward and independent of the sample value. The second term, however, depends on the sample value and hence needs the re-orientation. Its derivation requires the specification of a re-orientation scheme and the details are presented in the following section.

## 4 Applications

This section presents the details for two types of covariant images: fields of symmetric positive-definite matrices (SPD fields) and fields of Gaussian mixtures (GM fields). These two types of covariant images are fundamental in medical image analysis applications primarily in diffusion magnetic resonance imaging because, diffusivity of the water molecules in the tissues being imaged, a directional quantity of biological significance, can be compactly represented by them. In particular, their respective re-orientation schemes

### Algorithm 1 Optimization for $\Psi$ using Nonlinear Conjugate Gradient Method (NCG)

---

```

Initialize deformation fields :  $\gamma = Id$ 
Initialize family of coefficients :  $\mathcal{A} = 0$ 
Evaluate  $\frac{\partial}{\partial \mathcal{A}} Cost_{total}$  using Eq. 13 through Eq. 43
Set  $\mathbf{r}_0 \leftarrow -\frac{\partial}{\partial \mathcal{A}} Cost_{total}, k \leftarrow 0$ 
Set  $\mathbf{p}_0 \leftarrow -\mathbf{r}_0$ 
while  $Cost_{total_{k+1}}/Cost_{total_k} < (1 - \epsilon)$  do
  Compute  $\alpha_k$  and set  $\mathcal{A}_{k+1} = \mathcal{A}_k + \alpha_k \mathbf{p}_k$ ;
  Evaluate deformation fields using Eq. 12
  and its Jacobian;
  Interpolate  $I_2$  and its first order derivatives;
  Reorient  $I_1$ ;
  Evaluate  $\frac{\partial}{\partial \mathcal{A}} Cost_{total}$  using Eq. 13 through Eq. 43;
   $\mathbf{r}_{k+1} \leftarrow -\frac{\partial}{\partial \mathcal{A}} Cost_{total}$ ;
   $\beta_{k+1} \leftarrow \frac{\mathbf{r}_{k+1}^T \mathbf{r}_{k+1}}{\mathbf{r}_k^T \mathbf{r}_k}$ ;
   $\mathbf{p}_{k+1} \leftarrow -\mathbf{r}_{k+1} + \beta_{k+1} \mathbf{p}_k$ ;
   $\alpha_{k+1} = \alpha_k \frac{\mathbf{r}_{k+1}^T \mathbf{p}_k}{\mathbf{r}_{k+1}^T \mathbf{p}_{k+1}}$ ;
   $k \leftarrow k + 1$ ;
end while

```

---

often reflect the ways directional information are encoded by the images and utilized by the applications. For the two basic re-orientation schemes, the Preservation of Principal Direction (PPD) scheme (Cao et al. 2006; Alexander et al. 2001; Cheng et al. 2009) and the Finite Strain (FS) scheme (Alexander et al. 2001), SPD fields will be re-oriented using the latter scheme while GM fields will follow the former. In general, the FS scheme is used when all the eigenvectors of the SPD matrix (2nd order tensor) need to be re-oriented when undergoing a deformation. On the other hand, the PPD scheme considers only re-orientation of the first principle direction; this approach is valid when assuming a tubular structure for the axonal fibers in HARDI data sets, and this is the assumption we make for the GM fields in this paper. More details are provided in following sections and in Cheng et al. (2009).

For each covariant image, we will discuss the (Riemannian) metric used for matching the images as well as the specific re-orientation scheme. The latter will then provide us with the necessary information to complete the formulas for computing the gradient of the matching objective function.

#### 4.1 Diffusion Tensor (SPD) Fields

In diffusion magnetic resonance (MR) imaging, the diffusivity of water molecules at a given location is often represented by a symmetric positive-definite (SPD) matrix, with positive-definiteness ensuring positivity of the function. In addition to this important example, SPD fields also appear frequently in Computer Vision in the form of image structure tensors that are important for many Vision applications such as texture classification. In addition to the structure tensors considered as a feature transform of an image, there are other examples

of feature transforms that transform an image into an SPD field. One example we will investigate experimentally in the following section is to transform a (gray-scale) image into an SPD field given by the Riemannian metric tensor of its image graph. The motivation underlying this particular feature transform is to capture local information of an image using metric tensor of its image graph.

The sample-value space for SPD fields is the space  $\mathbb{P}(3)$  of 3-by-3 symmetric positive-definite matrices. Although not a vector space,  $\mathbb{P}(3)$  is convex and it admits a transitive action of  $\mathbf{GL}(3)$ , nonsingular 3-by-3 matrices: for  $\mathbf{X} \in \mathbb{P}(3)$ ,  $\mathbf{A} \in \mathbf{GL}(3)$ ,  $\mathbf{X} \rightarrow \mathbf{A}^\top \mathbf{X} \mathbf{A}$ . It is well-known that there is a canonical  $\mathbf{GL}$ -invariant metric on  $\mathbb{P}(3)$  [see Moakher (2006)].

This metric has been studied extensively in differential geometry, and in particular, its (squared) geodesic distance for two points in  $\mathbb{P}(3)$  can be computed exactly using the formula

$$\text{Dist}_F^2(\mathbf{I}_1, \mathbf{I}_2) = \text{Tr}(\log(\mathbf{I}_1^{-1/2} \mathbf{I}_2 \mathbf{I}_1^{-1/2})^2), \tag{18}$$

where  $\text{Tr}$ ,  $\log$  denote the matrix trace and logarithm functions, respectively.

#### 4.1.1 Re-orientation Scheme

In this paper, we use the finite strain (FS) method to re-orient the SPD matrices when the coordinates undergo a non-rigid deformation. As we will show in following section, we generate the SPD fields from 3-D gray scale MRI brain images, and the entries of the SPD matrices are related to the gradients of the intensities in three orthogonal directions. Therefore, all eigenvectors should be re-oriented properly. We use the FS method in Alexander et al. (2001), however in our work we express deformation vector fields in a DSC basis. Therefore the gradient w.r.t. the re-orientation is modified accordingly. For the FS scheme, the action of the Jacobian  $\mathbf{J}_\gamma$  of  $\gamma$  on the sample value is modeled after the  $\mathbf{GL}(3)$ -action above. More specifically, let  $\mathbf{J}_\gamma = \mathbf{U} \mathbf{D} \mathbf{V}^\top$  denote the singular value decomposition of  $\mathbf{J}_\gamma$ . The sample value  $\mathbf{I} \in \mathbb{P}(3)$  is transformed by  $\mathbf{J}_\gamma$  using the rotation  $\mathbf{R}$

$$\mathbf{I} \rightarrow \mathbf{R}^\top \mathbf{I} \mathbf{R},$$

where  $\mathbf{R} = \mathbf{U} \mathbf{V}^\top$ . Geometrically, the effect of the re-orientation by  $\mathbf{R}$  is to rotate the eigenvectors of  $\mathbf{I}$  without changing their associated eigenvalues.

#### 4.1.2 Metric for $\mathbb{P}(3)$

With this re-orientation scheme, it is then natural to consider the canonical invariant Riemannian metric on  $\mathbb{P}(3)$ . For an SPD field  $\mathbf{X}$

$$\mathbf{X} : (u, v, w) \rightarrow (\mathbf{r}, \mathbf{I}(\mathbf{r})), \tag{19}$$

where  $\mathbf{I}(\mathbf{r}) \in \mathbb{P}(3)$ , the Riemannian metric tensor  $\mathbf{K}_{\text{SPD}}$  of its image graph (Eq. 3) is given by the following formula (Gur and Sochen 2009)

$$\begin{pmatrix} 1 + \text{Tr}(\mathbf{M}_u^2) & \text{Tr}(\mathbf{M}_u) \text{Tr}(\mathbf{M}_v) & \text{Tr}(\mathbf{M}_u) \text{Tr}(\mathbf{M}_w) \\ \text{Tr}(\mathbf{M}_v) \text{Tr}(\mathbf{M}_u) & 1 + \text{Tr}(\mathbf{M}_v^2) & \text{Tr}(\mathbf{M}_v) \text{Tr}(\mathbf{M}_w) \\ \text{Tr}(\mathbf{M}_w) \text{Tr}(\mathbf{M}_u) & \text{Tr}(\mathbf{M}_w) \text{Tr}(\mathbf{M}_v) & 1 + \text{Tr}(\mathbf{M}_w^2) \end{pmatrix},$$

where  $\mathbf{M}_u = \mathbf{I}^{-1} \mathbf{I}_u$ ,  $\mathbf{M}_v = \mathbf{I}^{-1} \mathbf{I}_v$ , and  $\mathbf{M}_w = \mathbf{I}^{-1} \mathbf{I}_w$ . Using the above formulas for re-orientation and the Riemannian distance, we have,

$$\text{Dist}_F^2(\mathbf{I}_1, (\mathbf{I}_2 \circ \gamma)_{\mathcal{R}}) = \text{Tr}(\log(\mathbf{I}_1^{-1/2} \mathbf{R}^\top (\mathbf{I}_2 \circ \gamma) \mathbf{R} \mathbf{I}_1^{-1/2})^2). \tag{20}$$

#### 4.1.3 Gradient Computation

Setting  $\otimes = \mathbf{I}_1^{-1/2} \mathbf{R}^\top (\mathbf{I}_2 \circ \gamma) \mathbf{R} \mathbf{I}_1^{-1/2}$ , the first-order derivative of Eq. 20 can be written as

$$\begin{aligned} & \frac{\partial}{\partial \mathcal{A}_{nml}} \text{Dist}_F^2(\mathbf{I}_1, (\mathbf{I}_2 \circ \gamma)_{\mathcal{R}}) \\ &= \text{Tr} \left( 2 \log(\otimes) \frac{1}{\otimes} \frac{\partial \otimes}{\partial \mathcal{A}_{nml}} \right), \end{aligned} \tag{21}$$

where  $\frac{1}{\otimes} = \otimes^{-1}$  and

$$\begin{aligned} \frac{\partial \otimes}{\partial \mathcal{A}_{nml}} &= \mathbf{I}_1^{-1/2} \left( \frac{\partial \mathbf{R}^\top}{\partial \mathcal{A}_{nml}} (\mathbf{I}_2 \circ \gamma) \mathbf{R} \right. \\ & \quad \left. + \mathbf{R}^\top \frac{\partial (\mathbf{I}_2 \circ \gamma)}{\partial \mathcal{A}_{nml}} \mathbf{R} + \mathbf{R}^\top (\mathbf{I}_2 \circ \gamma) \frac{\partial \mathbf{R}}{\partial \mathcal{A}_{nml}} \right) \mathbf{I}_1^{1/2}. \end{aligned} \tag{22}$$

In Eq. 22,  $\partial(\mathbf{I}_2 \circ \gamma) / \partial \mathcal{A}_{nml}$  is simply

$$\frac{\partial (\mathbf{I}_2 \circ \gamma)}{\partial \mathcal{A}_{nml}} = \frac{\partial \mathbf{I}_2}{\partial u} \Big|_{u+U} \Phi_{U_{nml}}. \tag{23}$$

However, the first order derivative of  $\mathbf{R}$  w.r.t.  $\mathcal{A}_{nml}$  requires more algebra. The term can be written as

$$\frac{\partial \mathbf{R}}{\partial \mathcal{A}_{nml}} = \sum_{i,j} \frac{\partial \mathbf{R}}{\partial \mathbf{J}_{\gamma ij}} \frac{\partial \mathbf{J}_{\gamma ij}}{\partial \mathcal{A}_{nml}}, \tag{24}$$

where  $i$  and  $j$  are matrix indexes of  $\mathbf{J}_\gamma$  and from the definition of the Jacobian it is clear that

$$\begin{aligned} \frac{\partial \mathbf{R}}{\partial \mathcal{A}_{nml}} &= \frac{\partial \mathbf{R}}{\partial \mathbf{J}_{\gamma 11}} \frac{\partial \Phi_{U_{nml}}}{\partial u} \\ & \quad + \frac{\partial \mathbf{R}}{\partial \mathbf{J}_{\gamma 12}} \frac{\partial \Phi_{U_{nml}}}{\partial v} + \frac{\partial \mathbf{R}}{\partial \mathbf{J}_{\gamma 13}} \frac{\partial \Phi_{U_{nml}}}{\partial w}. \end{aligned} \tag{25}$$

For the evaluation of  $\partial \mathbf{R} / \partial \mathbf{J}_{\gamma ij}$  we refer the reader to Alexander et al. (2001). Evaluating gradient direction w.r.t. the DSC coefficients requires the integration of Eq. 21 over domain, and if we factor out basis functions in the expression of Eqs. 21 and 22, we can simplify the numerical scheme for the integration. For this factorization, we refer the reader to Appendices A and B respectively.

### 4.2 Gaussian Mixture Fields

With the multi-directional measurements from high angular resolution diffusion-weighted MRIs (HARDI), Tuch (2002) proposed to model the diffusion signals using a discrete mixture of Gaussians, and subsequent work by Jian et al. (e.g., Jian and Vemuri 2007) has made Gaussian mixture fields (GM fields) a useful class of image representations for HARDI data. Recall that a Gaussian mixture is a probability distribution that is the sum of a finite set of Gaussian distributions. For HARDI applications, a Gaussian mixture with a fixed number of components is associated with each voxel, and the  $n$ -component Gaussian mixture associated to a voxel positioned at  $\mathbf{r}$  provides a probability distribution  $\rho_{\mathbf{r}}$  representing the local diffusivity profile at the voxel,

$$\rho_{\mathbf{r}}(\mathbf{r}') = \sum_{i=1}^n \eta_i(\mathbf{r}) G(\mathbf{r}'; \cdot, 0, \Sigma_i(\mathbf{r})), \tag{26}$$

where  $G(\mathbf{r}'; \cdot, 0, \Sigma_i(\mathbf{r}))$  is the Gaussian distribution with zero mean and covariance matrix  $\Sigma_i$  with non-negative weights  $\eta_i(\mathbf{r})$  that sum to one. We note that the RHS is a distribution with  $\mathbf{r}'$  as the random variable, where  $\mathbf{r}'$  is the position vector with origin at the center of the voxel. The set of these Gaussian mixtures is considered as a discrete spatial sample of a underlying continuous Gaussian mixture field. In particular, a GM field  $\mathbf{I}$  is a covariant image with  $\mathbb{GM}(n)$ , the space of  $n$ -component Gaussian mixtures, as its sample-value space:

$$\mathbf{I}(\mathbf{r}) = \sum_{i=1}^n \eta_i(\mathbf{r}) G(\mathbf{r}'; \cdot, 0, \Sigma_i(\mathbf{r})). \tag{27}$$

For applications of HARDI data, there are two additional requirements: First, the covariant matrices  $\Sigma_i(\mathbf{r})$  are globally constant, i.e., independent of  $\mathbf{r}$ . Second, the cylindrical nature of the directional modeling in applications requires that the covariance matrix  $\Sigma_i(\mathbf{r})$  has at most two distinct eigenvalues.

#### 4.2.1 Metric for $\mathbb{GM}(n)$

We will use the  $L^2$ -metric on  $\mathbb{GM}(n)$  and for two elements  $\mathbf{I}_1, \mathbf{I}_2 \in \mathbb{GM}(n)$ , the  $L^2$ -distance between the two Gaussian mixtures  $\mathbf{I}_1, \mathbf{I}_2$  is

$$\text{Dist}_F^2(\mathbf{I}_1, \mathbf{I}_2) = \int_{\mathbb{R}^3} (\mathbf{I}_1 - \mathbf{I}_2)^2 d\mathbf{r}'. \tag{28}$$

The advantage of the  $L^2$ -distance for GM fields is that the squared distance can be computed using a closed-form formula. More specifically, the covariance matrix can be decomposed as

$$\Sigma = (\lambda_1 - \lambda_2) \mathbf{u} \mathbf{u}^T + \lambda_2 \mathbf{I}, \tag{29}$$

where the eigenvalues are  $\lambda_1 \geq \lambda_2 = \lambda_3$  with  $\mathbf{u}$  the (unit) principal eigenvector and  $\mathbf{I}$  the identity matrix. That is, we assume the tubular fiber structure in the HARDI data sets (Cheng et al. 2009). Then, given two Gaussian mixtures,  $\mathbf{I}_1$  and  $\mathbf{I}_2$  having weights  $\eta_i$  and  $\rho_i$ , and covariance matrices  $\Sigma_i$  and  $\Gamma_i$ , respectively, with eigenvalues  $\{\lambda_i\}_{i=1}^3$  and  $\{\zeta_i\}_{i=1}^3$ , and principal eigenvectors  $\mathbf{u}$  and  $\mathbf{v}$ , respectively, where  $i \in \{1, 2, \dots, n\}$ , Eq. 28 can be easily shown (Cheng et al. 2009) to be

$$\text{Dist}_F^2(\mathbf{I}_1, \mathbf{I}_2) = \boldsymbol{\eta}^T \mathbf{A} \boldsymbol{\eta} + \boldsymbol{\rho}^T \mathbf{B} \boldsymbol{\rho} - 2 \boldsymbol{\eta}^T \mathbf{C} \boldsymbol{\rho}, \tag{30}$$

where  $\boldsymbol{\eta} = (\eta_1, \dots, \eta_n)$  and  $\boldsymbol{\rho} = (\rho_1, \dots, \rho_n)$  are vectors of the mixture weights and  $\mathbf{A}, \mathbf{B}$  and  $\mathbf{C}$  are matrices whose elements are

$$\begin{cases} A_{i_1, i_2} = ((2\pi)^3 \det(\Sigma_{i_1} + \Sigma_{i_2}))^{-1/2} \\ B_{j_1, j_2} = ((2\pi)^3 \det(\Gamma_{j_1} + \Gamma_{j_2}))^{-1/2} \\ C_{i, j} = ((2\pi)^3 \det(\Sigma_i + \Gamma_j))^{-1/2} \end{cases}$$

The term  $\det(\Sigma + \Gamma)$  in the equation above is readily evaluated using  $\det(\Sigma + \Gamma) = \alpha - \beta(\mathbf{u}^T \mathbf{v})$ , where  $\alpha = (\lambda_1 + \zeta_2)(\lambda_2 + \zeta_1)(\lambda_2 + \zeta_2)$  and  $\beta = (\lambda_1 - \lambda_2)(\zeta_1 - \zeta_2)(\lambda_2 + \zeta_2)$ .

The  $L^2$ -distance defines the inner-product for the tangent spaces of  $\mathbb{GM}(n)$  given by

$$\langle \partial_{\mu} \mathbf{I}_1(\mathbf{r}), \partial_{\nu} \mathbf{I}_1(\mathbf{r}) \rangle_{\mathbb{GM}} = \int_{\mathbb{R}^3} \partial_{\mu} \mathbf{I}_1(\mathbf{r}) \partial_{\nu} \mathbf{I}_1(\mathbf{r}) d\mathbf{r}', \tag{31}$$

with  $\partial_{\mu} \mathbf{I}_1, \partial_{\nu} \mathbf{I}_1$ , the two tangent vectors of  $\mathbb{GM}(n)$  at the point  $\mathbf{I}_1 \in \mathbb{GM}(n)$  ( $\mu, \nu \in \{u, v, w\}$  the coordinates in  $\mathbb{R}^3$ ). It then follows that the components of the metric tensor  $\mathbf{K}_{\mathbb{GM}}$  can be determined by the following formula

$$\langle \mathbf{X}_{\mu}, \mathbf{X}_{\nu} \rangle = \lambda \delta_{\mu\nu} + \int_{\mathbb{R}^3} \partial_{\mu} I(\mathbf{r}) \partial_{\nu} I(\mathbf{r}) d\mathbf{r}', \tag{32}$$

Due to the constant covariance matrix fields  $\Sigma_i(\mathbf{r})$ , we have

$$\partial_{\mu} I_{\mathbf{r}}(\mathbf{r}') = \sum_{i=1}^n (\partial_{\mu} \eta_i(\mathbf{r})) G(\mathbf{r}'; 0, \Sigma_i(\mathbf{r})), \tag{33}$$

and together with earlier formulas, we can rewrite Eq. 32 as

$$\begin{aligned} \langle \mathbf{X}_\mu, \mathbf{X}_\nu \rangle &= \lambda \delta_{\mu\nu} \\ &+ \sum_{i,j=1}^n \partial_\mu \eta_i \partial_\nu \eta_j \frac{1}{\sqrt{(2\pi)^3 \det(\Sigma_i + \Sigma_j)}}. \end{aligned} \tag{34}$$

#### 4.2.2 Re-orientation Scheme

Re-orienting a Gaussian mixture requires the re-orientation of the covariance matrix of each of its components. Since each covariance matrix has one dominant eigenvalue, it suffices to re-orient only the corresponding principal direction, giving the so called Preservation of Principle Direction (PPD) scheme (Cheng et al. 2009). More precisely, for a component covariance matrix  $\Sigma$  given as in Eq. 29 with principal direction  $\mathbf{u}$ , its re-orientation  $\Sigma_{\mathcal{R}}$  under an image domain transform  $\gamma$  and its Jacobian  $\mathbf{J}_\gamma$  is given by

$$\Sigma_{\mathcal{R}} = (\lambda_1 - \lambda_2) \mathbf{u}_R \mathbf{u}_R^\top + \lambda_2 \mathbf{I}, \tag{35}$$

where the re-oriented principal direction  $\mathbf{u}_R$  is given by

$$\mathbf{u}_R = \frac{\mathbf{J}_\gamma \mathbf{u}}{|\mathbf{J}_\gamma \mathbf{u}|}. \tag{36}$$

For a GM field given in Eq. 27, its re-orientation is defined by the re-orientations of its components:

$$I_1(\mathbf{r})_{\mathcal{R}} = \sum_{i=1}^n \eta_i(\mathbf{r}) G(\mathbf{r}'; 0, \Sigma_{i\mathcal{R}}(\mathbf{r})). \tag{37}$$

#### 4.2.3 Gradient Computation

With the reorientation given above, Eq. 30 is rewritten as

$$\begin{aligned} \text{Dist}_F^2(I_{1\mathcal{R}}, I_2 \circ \gamma) &= \boldsymbol{\eta}^\top \mathbf{A}_{\mathcal{R}} \boldsymbol{\eta} + (\boldsymbol{\rho} \circ \gamma)^\top \mathbf{B} (\boldsymbol{\rho} \circ \gamma) \\ &- 2 \boldsymbol{\eta}^\top \mathbf{C}_{\mathcal{R}} (\boldsymbol{\rho} \circ \gamma), \end{aligned} \tag{38}$$

Then, we can write its first order derivative w.r.t  $\mathcal{A}_{nml}$  as

$$\begin{aligned} &\frac{\partial}{\partial \mathcal{A}_{nml}} \text{Dist}_F^2(I_{1\mathcal{R}}, I_2 \circ \gamma) \\ &= \boldsymbol{\eta}^\top \frac{\partial \mathbf{A}_{\mathcal{R}}}{\partial \mathcal{A}_{nml}} \boldsymbol{\eta} + 2(\boldsymbol{\rho} \circ \gamma)^\top \mathbf{B} \frac{\partial(\boldsymbol{\rho} \circ \gamma)}{\partial \mathcal{A}_{nml}} \\ &- 2 \boldsymbol{\eta}^\top \frac{\partial \mathbf{C}_{\mathcal{R}}}{\partial \mathcal{A}_{nml}} (\boldsymbol{\rho} \circ \gamma) - 2 \boldsymbol{\eta}^\top \mathbf{C}_{\mathcal{R}} \frac{\partial(\boldsymbol{\rho} \circ \gamma)}{\partial \mathcal{A}_{nml}}, \end{aligned} \tag{39}$$

where

$$\left. \frac{\partial \mathbf{A}_{\mathcal{R}}}{\partial \mathcal{A}_{nml}} \right|_{i,j} = \beta \frac{\mathbf{u}_{i\mathcal{R}}^\top \mathbf{u}_{j\mathcal{R}} [\partial(\mathbf{u}_{i\mathcal{R}}^\top \mathbf{u}_{j\mathcal{R}}) / \partial \mathcal{A}_{nml}]}{(2\pi \det(\Sigma_{i\mathcal{R}} + \Sigma_{j\mathcal{R}}))^{3/2}} \tag{40}$$

$$\left. \frac{\partial \mathbf{C}_{\mathcal{R}}}{\partial \mathcal{A}_{nml}} \right|_{i,j} = \beta \frac{\mathbf{u}_{i\mathcal{R}}^\top \mathbf{v}_j [\partial(\mathbf{u}_{i\mathcal{R}}^\top \mathbf{v}_j) / \partial \mathcal{A}_{nml}]}{(2\pi \det(\Sigma_{i\mathcal{R}} + \Gamma_j))^{3/2}} \tag{41}$$

$$\left. \frac{\partial(\boldsymbol{\rho} \circ \gamma)}{\partial \mathcal{A}_{nml}} \right|_{u+U} = \frac{\partial \boldsymbol{\rho}}{\partial u} \Big|_{u+U} \Phi_{U_{nml}} \tag{42}$$

and

$$\begin{aligned} \frac{\partial \mathbf{u}_{i\mathcal{R}}}{\partial \mathcal{A}_{nml}} &= \mathbf{J}^{-1} \left( \frac{\partial \mathbf{J}}{\partial \mathcal{A}_{nml}} \right) \mathbf{u}_{i\mathcal{R}} \\ &- \left[ \mathbf{u}_{i\mathcal{R}}^\top \mathbf{J}^{-1} \left( \frac{\partial \mathbf{J}}{\partial \mathcal{A}_{nml}} \right) \mathbf{u}_{i\mathcal{R}} \right] \mathbf{u}_{i\mathcal{R}} \end{aligned} \tag{43}$$

We present how to factor out the basis functions from Eq. 39 in Appendix 2.

## 5 Experiments

In this section, we present three experiments and their results, demonstrating the effectiveness of the similarity measure  $\mathbf{S}(\mathbf{X}, \mathbf{Y})$  for covariant images in two very specific medical imaging applications. In the first experiment, we evaluate the effectiveness of the optimization method outlined in the previous section for computing image matching, using the Diffeomorphic Demons (Vercauteren et al. 2007), a registration method popular in medical imaging community, as the main comparison. In the second and third experiments, we use  $\mathbf{S}(\mathbf{X}, \mathbf{Y})$  as the main pairwise similarity measure for 3D MR brain image classification based on the age and disease status (Alzheimer’s disease) of the patient, and for seizure detection in rat brains using High Angular Resolution Diffusion-Weighted Imaging (HARDI), respectively.

### 5.1 Synthetic Data

In this experiment, we evaluate the accuracy of the matching computed by minimizing the objective function  $\mathbf{E}(\gamma; \mathbf{X}_1, \mathbf{X}_2)$ , and compare our result with that of Diffeomorphic Demons (Vercauteren et al. 2007; Kroon et al. 2009). Specifically, five 2D slices of 3D brain MRI scans are randomly chosen from the OASIS database (Marcus et al. 2007) and image domain diffeomorphisms are generated and used as the ground truth for evaluating the accuracy. The test set of synthetic diffeomorphisms is prepared in following way: (1) To pick control points and generate vectors at the points from a Gaussian distribution. (2) To interpolate these vectors to other pixels. Diffeomorphisms are checked by checking

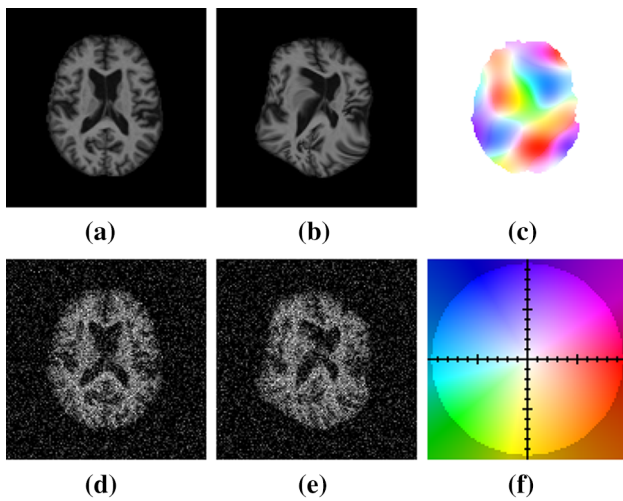


**Fig. 4** Example images and transforms used in the synthetic data experiment: **a** original image, **b** deformed image, **c** color-coded deformation vector field with encoding scheme shown in **f**. Color coding used to display the flow vectors is the one standardly used to display optical flow fields, see <http://vision.middlebury.edu/flow/eval/results/results-a1.php>. The 'tick marks' on the axes depict a flow unit in one pixel. **d** and **e** are images of **(a)** and **(b)** with additional Gaussian noise ( $\sigma = 0.02$ )

if there is any folding and the determinants of Jacobian are positive.

In this experiment, we use the gray-scale images without re-orientation, and the purpose is the evaluation of only the matching component of our method. The diffeomorphically deformed images are subject to additional Gaussian white noise with examples shown in Fig. 4. For quantitative comparisons, the angle error (AE) and the end-point error (EPE) are computed between the ground truth and the computed deformation vector fields within the regions of interest (ROI). For implementation of the Demons algorithm, we used the code provided by the authors of Kroon et al. (2009). To achieve best results with the code, we tuned the regularization parameter (used in this algorithm) in the range (0.01–0.9) for the best results. Best result here refer to a registration that yielded the smallest energy cost satisfying no-folding in the deformed mesh and one that has a positive determinant of Jacobian. For all the experiments, the image intensity was scaled by 255. The results are shown in Table 1 and Fig. 6, with several visual comparisons also shown in Fig. 5. The deformation field is color coded using standard color coding used to display flow fields in the Computer Vision community. More specifically, the angle of each vector is represented with hue which has value between 0° and 360° and the length of each vector is represented with saturation which is rescaled w.r.t. the maximum length of vector in vector field. The 'tick marks' on the axes depict a flow unit in one pixel. For more details on this color coding scheme, we refer the reader to Baker et al. (2011) and

**Table 1** Accuracy comparison using the angle error (AE) and the Euclidean distance (ED) between the ground truth deformation vector fields and the ones computed by our method and the diffeomorphic Demons respectively

	Original images		Gaussian noise $\sigma = 0.0001$		Gaussian noise $\sigma = 0.001$		Gaussian noise $\sigma = 0.005$		Gaussian noise $\sigma = 0.01$		Gaussian noise $\sigma = 0.02$	
	AE	ED	AE (avg)	ED (avg)	AE (avg)	ED (avg)	AE (avg)	ED (avg)	AE (avg)	ED (avg)	AE (avg)	ED (avg)
pSNR( <i>dB</i> )			41.63–41.84	31.70–31.83	24.74–25.02	21.80–21.93	18.98–19.11					
Error measure												
Our method	0.0064	0.0276	0.0588	0.2445	0.0650	0.2726	0.1031	0.4217	0.1599	0.6679	0.2840	1.1880
Diffeomorphic Demons	0.0444	0.1957	0.1129	0.4516	0.2040	0.8427	0.4050	1.4215	0.3988	1.6363	0.4765	1.9237

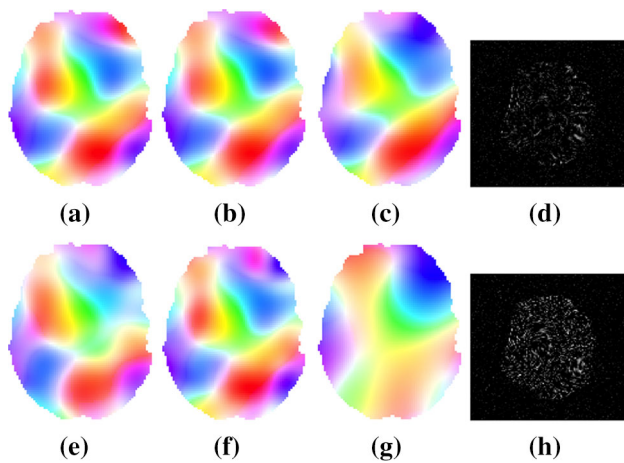


**Fig. 5** Visual comparisons between deformation fields computed by Diffeomorphic Demons and our method. The ground truth deformation is shown in Fig. 4c. **a–c** Display the deformation vector fields computed by our method for the deformed image shown in Fig. 4b and with added Gaussian noise of  $\sigma = 0, 0.0001, 0.02$ , respectively. **e–g** Display the deformation vector fields computed by Diffeomorphic Demons for the same deformed image and with added Gaussian noise of  $\sigma = 0, 0.0001, 0.02$ , respectively. **d** and **h** show intensity differences between a target and registered images with our method and Demons respectively. Gaussian noise of  $\sigma = 0.001$  was added to the source and target. In this comparison, the bitmap values are doubled to enhance visual effect

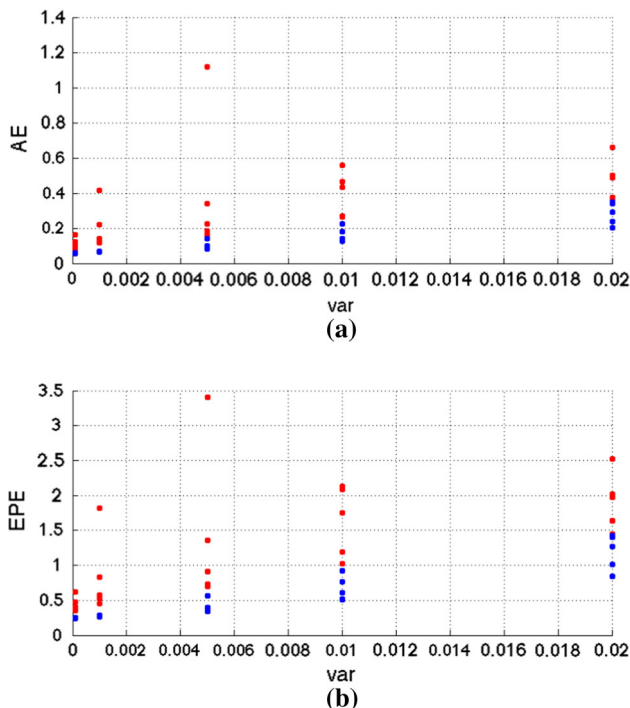


**Fig. 6** Plots of error measures. **a** The angular error (AE) and **b** the end-point error (EPE). The horizontal axis represents the variance of the Gaussian noise. The errors from the diffeomorphic Demons and our approach are depicted in red and blue, respectively. From the plots, it is clear that our method generally produces more accurate results than the diffeomorphic Demons

the web-site <http://vision.middlebury.edu/flow/eval/results/results-a1.php>. These results demonstrate that our method outperforms the Diffeomorphic Demons using AE and EPE as the error measures. In particular, across the images chosen for the experiment, the errors incurred by our method are consistently smaller than the ones from the Demons algorithm as depicted in Fig. 6.

For the next two experiments, we will use  $\mathbf{S}(\mathbf{X}_1, \mathbf{X}_2)$  as the similarity measure in a supervised learning setting—in following the SPD fields and Gaussian mixture field examples, measuring similarity requires pairwise registration and it takes less than 1min for each pair of subjects with same machine configuration specified in Sect. 3.3. More specifically, the similarity  $\mathbf{S}(\mathbf{X}_1, \mathbf{X}_2)$  will be used in conjunction with the diffusion map for dimensionality reduction of the image data. In the low-dimensional Euclidean space—which is 8-dimensional in our case—determined by the diffusion map using  $\mathbf{S}(\mathbf{X}_1, \mathbf{X}_2)$  as its affinity measure, the classification is carried out using the nearest neighbor method with the standard Euclidean distance. For details regarding diffusion maps, we refer the reader to the original work of Coifman et al. (2005), Coifman and Lafon (2006).

## 5.2 Classifications of 3D MR Brain Images

### 5.2.1 Data Preparation and Experimental Setting

The OASIS dataset (Marcus et al. 2007) contains 3D MR (gray-scale) brain images of 416 humans aged between 18 and 92. Each subject is associated with several attributes that include age and possible disease status, e.g., Alzheimer’s disease (AD) patient. The classification problems of interest are to classify MR brain images according to their age groups and their disease status. Specifically, we divide the subjects into three age groups: Young (<41), Middle-aged (41–60), Old (>60). Furthermore, there are also two additional groups of Alzheimer’s disease patients and normal subjects (the control group). In this experiment, we will show that a straightforward classification using the original gray-scale MR images and registration does not provide satisfactory results. However, superior results can be obtained by transforming the gray-scale images into covariant images that are SPD fields. Specifically,

- 1 The image graphs of the OASIS MR (gray-scale) images are constructed in  $\mathbb{R}^3 \times \mathbb{R}_+$ .
- 2 For each image graph, the Riemannian metric tensor (first fundamental form) represented as a symmetric positive-definite matrix is computed at each voxel. This transforms each gray-scale image into a covariant image  $\mathbf{X}$ , an SPD field.

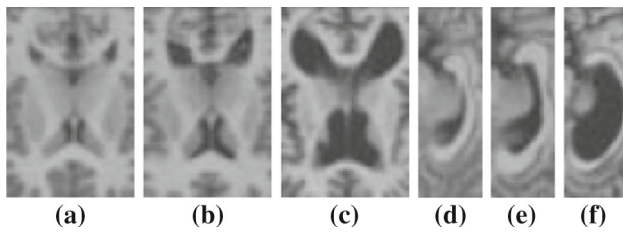


**Fig. 7** Slices of 3-D MRI images. **a–c** Cross-sectional images of the ventricles of 18, 43, and 81 year old respectively. **d–f** Longitudinal images of the ventricles in the same order

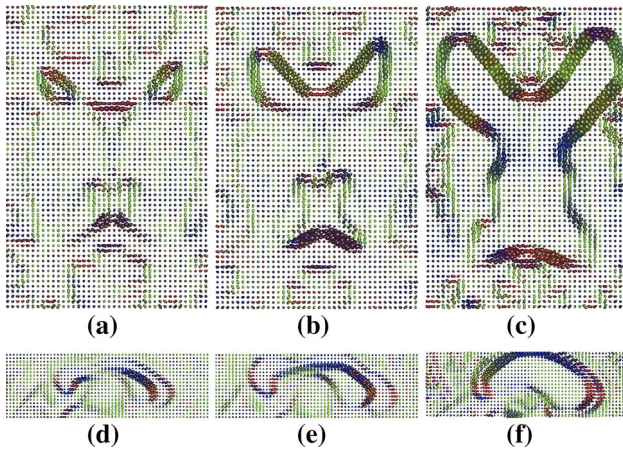


**Fig. 8** Slices of the 3-D SPD tensor-valued images that are the first fundamental forms of the image graphs of the ventricles shown in Fig. 7. Each SPD tensor-valued image is visualized as a field of spherical functions [Bampoutis et al. \(2007\)](#). **a–c** 2-D slices from the superior view of 18, 43, and 81 year olds, respectively. **d–f** Mid-sagittal sections of the ventricles in the same order

We choose the ventricles as the main ROIs for computing the similarity since this particular anatomical structure is known to be important for age classification. Figures 7 and 8 show 2D slices of longitudinal and cross-sectional OASIS MR images and their corresponding SPD fields. Figure 9 displays several (2D) dimensionality reduction results for dif-

ferent pairs of age groups. The separations between different age groups are clearly visible, indicating the appropriateness of the similarity measure  $S(X_1, X_2)$  for age classification. For classification, we use both the leave-one-out method and four-fold cross-validation for selecting training and test images. For the Alzheimer’s disease patient classification, we took seventy subjects from the Old age group with 35 subjects diagnosed as AD patients and 35 normal subject as the control. The classification is performed similarly using leave-one-out and four-fold cross-validation.

5.2.2 Results and Discussion

The experimental results are summarized in Tables 2, 3, and 4, and there are four specific objectives investigated in this set of experiments:

- 1 Achievable classification result using our method,
- 2 Improvement over Diffeomorphic Demons,
- 3 Relevance and importance of the re-orientation and metric,
- 4 Comparisons with other similar classification results published in recent literature.

In general, the regularization parameter,  $L_r$  can be chosen using the standard cross-validation approach ([Bates et al. 1987](#)), but in our experiments, we picked it empirically by experimenting with several values and choosing the one that gave the best performance in terms of classification scores. In Table 2, we present sample test results that we have used to pick a best  $L_r$ . In this test, we picked 39 of young and 49 of old brains from OASIS dataset, and validation method is the standard leave-one-out technique.

Table 2 reflects the fact that the standard deviation of the Score—which is 1.8—is small compared to the one in  $L_r$ —which is 3.16 (as  $L_r$  values are multiplied by 100). This indicates that the classification scores are relatively less sensitive

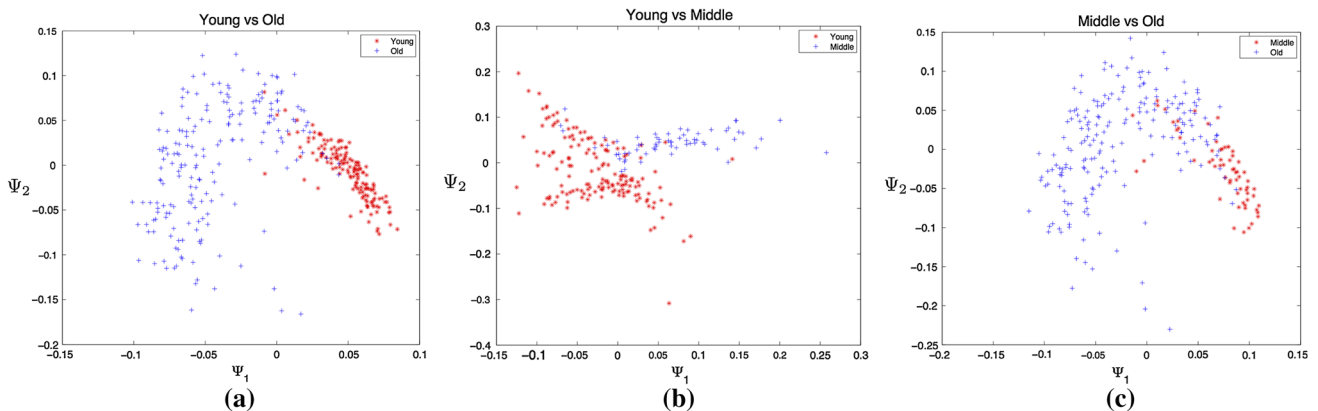


**Fig. 9** 2-D plots of the dimensionality reduction results using diffusion map: **a** young versus old, **b** young versus middle, and **c** middle versus old

**Table 2** Classification results of sample test of young versus old with various penalty parameters

$L_r$	0.01	0.03	0.05	0.07	0.09
Score	100 %	97.72 %	98.86 %	96.59 %	95.45 %

to variations in the value of  $L_r$ . Hence, we choose to pick the value of  $L_r (= 0.01)$  empirically rather than use the standard cross-validation approach (Bates et al. 1987).

Table 2 reports the classification results obtained using our method and correspondingly, Table 3 reports the results obtained using Demons algorithm that operates directly on the gray-scale MR images using the sum-of-squares (SSD) as the matching cost function. The classification method and validation scheme used in both experiments are identical except that Demons method does not transform the gray-scale images into covariant images and it uses the SSD as its similarity measure. The observed improvements of our method over Demons (higher classification rates with smaller variances) visible from the two tables can primarily be attributed to the use of covariant images and the similarity measure  $S(\mathbf{X}_1, \mathbf{X}_2)$  in our method.

Next, we demonstrate the flexibility of our approach by varying the ambient metric. For Table 3, the metric in the total space  $E$  is the product metric of Euclidean metric on  $\mathbb{R}^3$  and the affine-invariant metric on  $\mathbb{P}(3)$ . Alternatively, we can consider sample-value space  $\mathbb{P}(3)$  as a convex subset of  $\mathbb{R}^6$ , giving the mapping  $\mathbf{X} : \mathbb{R}^3 \rightarrow \mathbb{R}^3 \times \mathbb{R}^6$ , and we replace the affine-invariant metric with the Euclidean metric in  $\mathbb{R}^6$ , i.e., the Frobenius norm. Table 5 reports the results using the Euclidean metric (with and without re-orientation) for the classification of young versus old age groups. In the last column of Table 5, we have used the affine-invariant Riemannian distance in  $\mathbb{P}(3)$  but with the standard Lebesgue measure in  $\mathbb{R}^3$  as the integral measure.

The comparison between Table 3 and the first two columns of Table 5 shows that the affine-invariant metric on  $\mathbb{P}(3)$  is superior to the Euclidean metric on  $\mathbb{R}^6$ , and as mentioned earlier, the affine-invariant metric is compatible with the re-

orientation while the Euclidean metric is not. Furthermore, the comparison between Table 3 and the third column of Table 5 indicates that using the Riemannian volume form derived from the covariant image graph as the integral measure produces better results than using the standard Euclidean volume form. In other words, the intrinsic geometry of the covariant image graph matters. We remark that the results in the third column of Table 5 are slightly better than the results obtained using the conventional intensity-value-based method reported in Table 4. This suggests that the feature transform that transforms a gray-scale image into an SPD covariant image may have imbued the covariant image with local geometric information that are useful for image matching and classification.

Finally, in Table 6, we have compared our results with previously published classification results using the OASIS dataset. Authors in Xie et al. (2010) register each image to a common atlas and compute the deformation tensor field as the main discriminating feature for each image. The deformation tensor fields are taken to be points in a high-dimensional feature space that is the Cartesian product of several  $\mathbb{P}(3)$ s, and the classification is based on the metric distance of the Cartesian product. In Chen et al. (2010), histograms of deformation vector fields have been used as features, and the CAVIAR method proposed in Chen et al. (2010) uses an adaboost-like approach in its classification by using a weighted combination of several weak learners/classifiers. We remark that the image matching methods used in these works are all  $L^2$ -based methods that compare only sample (intensity) values at corresponding voxels. Furthermore, our method compares favorably with these methods in terms of classification rates, and in particular, for the more challenging problem of classifying brain images of Alzheimer's disease (AD) patients, our method demonstrates a small but real improvement over CAVIAR and Adaboost (Chen et al. 2010). In AD versus control classification test, we select 35 of AD and 35 of old brains from full OASIS dataset, and same dataset has been used for CAVIAR and Adaboost classifiers. Resulting classification scores are also reported in Table 6. Authors in Xie et al. (2010), however, used different dataset for this AD test;

**Table 3** Classification results for the four-fold cross-validation experiment (first four rows) and the leave-one-out experiment (last row) using the proposed method

Input: 3-by-3 SPD image graphs	Old versus young (%)	Old versus middle (%)	Middle versus young (%)	AD versus control (%)
Maximum	100	100	100	100
Minimum	97.72	95.38	94.54	75.0
Average	99.54	98.98	98.54	94.87
Standard deviation	0.79	1.09	1.62	5.55
Leave-one-out	99.43	98.46	99.09	95.32

For the four-fold cross-validation experiment, training and test images are randomly generated fifty times, resulting in fifty different classification runs. The metric used for the ambient space  $\mathbb{R}^3 \times \mathbb{P}(3)$  is the product metric of the Euclidean metric on  $\mathbb{R}^3$  and the affine-invariant metric on  $\mathbb{P}(3)$

**Table 4** Classification results for the four-fold cross-validation experiment (first four rows) and the leave-one-out experiment (last row) using the Diffeomorphic Demons method

Input: image function	Old versus young (%)	Old versus middle (%)	Middle versus young (%)
Maximum	100	100	100
Minimum	96.59	93.85	85.45
Average	98.81	97.35	94.94
Standard deviation	0.88	2.065	2.96
Leave-one-out	98.3	97.69	97.27

In this experiment, the intensity values of the OASIS MRI images are used directly without feature transforming into SPD fields as in Table 3. The results reported here use exactly the same sets of training and testing data as in Table 3

**Table 5** Classification results for young versus old age groups using different metrics on the ambient space (with and without reorientation)

Methods	Frobenius with reorientation (%)	Frobenius without reorientation (%)	Riemannian distance with reorientation and standard volume form (%)
Maximum	100	100	100
Minimum	88	88.63	96.59
Average	94.96	96.52	99.03
Standard deviation	2.57	2.15	0.99
Leave-one-out validation	97.03	98.01	99.15

Results from the four-fold cross-validation experiment are shown in the first four rows and the leave-one-out experiment shown in the last row. In the first and second columns, the Frobenius norm is used as the metric for  $\mathbb{P}^3$  with integral measure derived from the Riemannian volume form of the image graph. In the last column, the metric for  $\mathbb{P}^3$  is the affine-invariant Riemannian metric using the volume form introduced in Tagare et al. (2009) as the integral measure

**Table 6** Classification results of our methods and four other published methods using four-fold cross-validation

	Old versus young	Old versus middle (%)	Middle versus young (%)	AD versus control (%)
Our Method	99.54	98.98	98.54	94.87
CAVIAR Chen et al. (2010)	99.14	98.36	97.76	88.0
Adaboost Chen et al. (2010)	98.75	96.80	96.0	84.38
Submanifold projection Xie et al. (2010)	96.43	90.23	84.32	.
Nearest Neighbor in PCA Xie et al. (2010)	92.43	87.74	78.42	.

therefore, the AD test results in Xie et al. (2010) are not reported here. In addition, we carried out the Hotelling’s T2 test with our feature vectors— which are in  $R^8$ — to determine the statistical significance of our classification in the AD test. The T2 test yielded a p-value less than 0.05. Therefore, the null-hypothesis was rejected. In addition, it leads us to conclude that the feature vectors that we have chosen are well suited for this classification problem.

### 5.3 Seizure Detection from High Angular Resolution Diffusion-Weighted MR Imaging (HARDI)

#### 5.3.1 Data Preparation and Experimental Setting

The dataset consists of HARDI data acquired from nine rat brains. The brains have undergone electrical stimulation for

inducing epileptic seizures. HARDI data are collected over several time intervals in order to observe occurrences of seizure from the time-sequence scans. For each rat, there are between five to eight temporal scans and we refer to data taken before seizure but post stimulation as pre-seizure and data collected after seizure is referred to as post-seizure. The aim of this experiment is to automatically classify the data into two classes namely, pre- and post-seizure classes respectively. Specifically, we have 34 pre-seizure and 12 post-seizure data sets. We acquired *in vivo* HARDI data of rat brains and computed the GM fields whose weight vector dimension is 46 and this is a sparse vector with the number of nonzero weights being equal to the number of fiber crossings in that voxel. The Gaussian mixture model is estimated using the tensor distribution model described in Jian et al. (2007), Jian and Vemuri (2007). In Jian et al. (2007),

**Table 7** Classification results for the leave-one-out validation experiment using two different matching methods

	GM fields as shapes		GM fields as functions	
	Pre-seizure (%)	Post-seizure (%)	Pre-seizure (%)	Post-seizure (%)
Score	100	75	91.18	50
Total score	93.47		80.43	

Classification (detection) results for pre- and post-seizure are reported separately

**Table 8** Average classification results for the four-fold validation experiment using 50 different sets of training and testing data

	Pre-seizure	Post-seizure	Pre- and Post-seizure
Ave. score	96.25 %	75.6 %	90.61%

Jian and Vemuri (2007), the Gaussian mixture model estimation requires solving a linear system of sparse weight vector whose dimension was set to 46 in this experimental set up. Therefore, the covariant images are GM fields with 46 dimensional weight vector—this leads to  $n = 46$  in Eq. 26—and their image graphs are constructed based on the mapping  $\mathbf{I} : \mathbb{R}^3 \rightarrow \mathbb{R}^3 \times \text{GM}(46)$ . The remaining experimental details are similar to the 3D MR brain image experiment above: using  $\mathbf{S}(\mathbf{X}_1, \mathbf{X}_2)$  as the similarity (affinity) measure and the diffusion map for dimensionality reduction. Classification is carried out using nearest neighbor method with the Euclidean metric in the low-dimensional feature space.

### 5.3.2 Results and Discussions

As in the previous experiment, we have used leave-one-out method and four-fold cross-validation for selecting training and testing data. The result from the leave-one-out validation is reported in Table 7 and the result is compared with the result obtained using the sum of squared difference cost function for image registration method but with the inclusion of re-orientation transform. The main difference is the use of Riemannian volume form as the integral measure in our method and the standard Lebesgue measure in  $\mathbb{R}^3$  in the comparative method, and this results in the noticeable difference between the two classification results. For the four-fold cross-validation experiment, we have randomly selected 8 of pre-seizure and 3 of post-seizure out of 34 and 12, respectively, as the test data. The random selection is performed 50 times as before, and the averaged classification results are reported in Table 8.

## 6 Conclusions

In this paper, we have proposed the novel notion of covariant images and a novel similarity measure for covariant images. Covariant images are images whose sample values are trans-

formed by the application of image domain transforms, and they play important roles in various medical image applications. We have argued that their covariant nature with respect to image domain transforms blur the distinction between image and sample-value domains, opening the door for the geometric approach advocated in this paper. In particular, using their image graphs, covariant images are considered as shapes embedded in an ambient space that is the Cartesian product of the image and sample-value domains, and the similarity between two covariant images are formulated as the similarity between their associated shapes. For their comparisons, we have proposed a matching framework that incorporates both extrinsic and intrinsic geometry of the covariant images. We have also developed an optimization method for efficiently computing the matching, and hence the similarity between two covariant images. The proposed similarity measure has been evaluated in two extensive sets of experiments on classifying human and animal brain images. Good classification results achieved in these two experiments have demonstrated its effectiveness and usefulness for brain image classifications, and its great potential for other medical image applications as well.

**Acknowledgments** This research was supported in part by NSF Grant IIS 0916001 to JH and BCV and the NIH grant NS066340 to BCV.

## Appendix 1

In this section, we show how to factor out DSC basis functions in formulating the gradient descent direction w.r.t. the DSC coefficients. Here, we only show details of derivatives w.r.t.  $\mathcal{A}_{nml}$ . Derivatives w.r.t.  $\mathcal{B}_{nml}$  and  $\mathcal{C}_{nml}$  can be done in the same way described in the following. In this section we consider Eq. 14 and in the following sections Eqs. 15 and Eq. 16 will be considered. Here, we only consider the image graphs of Gaussian mixture fields.

Equation 14 is rewritten as

$$\begin{aligned} & \frac{\partial}{\partial \mathcal{A}_{nml}} \text{Dist}^2(\mathbf{X}_{1\mathcal{R}}, \mathbf{X}_2 \circ \gamma) \\ &= \frac{\partial}{\partial \mathcal{A}_{nml}} (\underbrace{\lambda(U^2 + V^2 + X^2)}_{\text{Part1}} + \underbrace{\text{Dist}_F^2(I_{1\mathcal{R}}, I_2 \circ \gamma)}_{\text{Part2}}) \end{aligned} \quad (44)$$

In the *Part1* of Eq. 44, factoring out basis functions is very straight forward, therefore, we only show how to do this in the *Part2* below.

$$\begin{aligned} & \frac{\partial}{\partial \mathcal{A}_{nml}} \text{Dist}_F^2(I_1\mathcal{R}, I_2 \circ \gamma) \\ &= \boldsymbol{\eta}^\top \frac{\partial \mathbf{A}_{\mathcal{R}}}{\partial \mathcal{A}_{nml}} \boldsymbol{\eta} - 2\boldsymbol{\eta}^\top \frac{\partial \mathbf{C}_{\mathcal{R}}}{\partial \mathcal{A}_{nml}} (\boldsymbol{\rho} \circ \gamma) \\ & \quad + 2(\boldsymbol{\rho} \circ \gamma)^\top \mathbf{B} \frac{\partial (\boldsymbol{\rho} \circ \gamma)}{\partial \mathcal{A}_{nml}} - 2\boldsymbol{\eta}^\top \mathbf{C}_{\mathcal{R}} \frac{\partial (\boldsymbol{\rho} \circ \gamma)}{\partial \mathcal{A}_{nml}}, \end{aligned} \tag{45}$$

Factoring out basis functions in Eq. 45 requires evaluation Eqs. 40, 41, and 42 explicitly. First, we need to evaluated derivatives of Jacobian matrix,  $\mathbf{J}$ . Given

$$\mathbf{J} = \begin{pmatrix} 1 + U_u & U_v & U_w \\ V_u & 1 + V_v & V_w \\ W_u & W_v & 1 + W_w \end{pmatrix}, \tag{46}$$

the first order derivative w.r.t.  $\mathcal{A}_{nml}$  is given

$$\frac{\partial \mathbf{J}}{\partial \mathcal{A}_{nml}} = \begin{pmatrix} \frac{\partial}{\partial u} \Phi_{U_{nml}} & \frac{\partial}{\partial v} \Phi_{U_{nml}} & \frac{\partial}{\partial w} \Phi_{U_{nml}} \\ 0 & 0 & 0 \\ 0 & 0 & 0 \end{pmatrix}. \tag{47}$$

Once we notice that

$$\begin{aligned} & \frac{\partial \mathbf{J}}{\partial \mathcal{A}_{nml}} \mathbf{u}_{i\mathcal{R}} \\ &= \begin{pmatrix} \underbrace{u_{i\mathcal{R}1} \frac{\partial}{\partial u} \Phi_{U_{nml}} + u_{i\mathcal{R}2} \frac{\partial}{\partial v} \Phi_{U_{nml}} + u_{i\mathcal{R}3} \frac{\partial}{\partial w} \Phi_{U_{nml}}}_{\Delta_i} \\ 0 \\ 0 \end{pmatrix}, \end{aligned} \tag{48}$$

where the subscript  $i$  of  $\Delta$  is same with  $i$  of  $\mathbf{u}_{i\mathcal{R}}$ , and rewrite  $\mathbf{J}^{-1}$  as

$$\mathbf{J}^{-1} = \begin{pmatrix} J_{11}^{-1} & J_{12}^{-1} & J_{13}^{-1} \\ J_{21}^{-1} & J_{22}^{-1} & J_{23}^{-1} \\ J_{31}^{-1} & J_{32}^{-1} & J_{33}^{-1} \end{pmatrix} = \left( \mathbf{J}_1^{-1} \middle| \mathbf{J}_2^{-1} \middle| \mathbf{J}_3^{-1} \right) \tag{49}$$

then, we can factor out basis functions in Eq. 43 as

$$\frac{\partial \mathbf{u}_{i\mathcal{R}}}{\partial \mathcal{A}_{nml}} = (\mathbf{J}_1^{-1} - (\mathbf{u}_{i\mathcal{R}}^\top \mathbf{J}_1^{-1}) \mathbf{u}_{i\mathcal{R}}) \Delta_i \tag{50}$$

and in the same way,

$$\frac{\partial \mathbf{u}_{i\mathcal{R}}}{\partial \mathcal{B}_{nml}} = (\mathbf{J}_2^{-1} - (\mathbf{u}_{i\mathcal{R}}^\top \mathbf{J}_2^{-1}) \mathbf{u}_{i\mathcal{R}}) \Delta_i \tag{51}$$

$$\frac{\partial \mathbf{u}_{i\mathcal{R}}}{\partial \mathcal{C}_{nml}} = (\mathbf{J}_3^{-1} - (\mathbf{u}_{i\mathcal{R}}^\top \mathbf{J}_3^{-1}) \mathbf{u}_{i\mathcal{R}}) \Delta_i. \tag{52}$$

With Eq. 50, we can rewrite Eqs. 40 and 41 as

$$\begin{aligned} & \frac{\partial \mathbf{A}_{\mathcal{R}}}{\partial \mathcal{A}_{nml}} \Big|_{i,j} \\ &= a_{ij} \mathbf{u}_{i\mathcal{R}}^\top \mathbf{u}_{j\mathcal{R}} [\mathbf{u}_{i\mathcal{R}}^\top (\mathbf{J}_1^{-1} - (\mathbf{u}_{j\mathcal{R}}^\top \mathbf{J}_1^{-1}) \mathbf{u}_{j\mathcal{R}}) \Delta_j \\ & \quad + (\mathbf{J}_1^{-1} - (\mathbf{u}_{i\mathcal{R}}^\top \mathbf{J}_1^{-1}) \mathbf{u}_{i\mathcal{R}})^\top \mathbf{u}_{j\mathcal{R}} \Delta_i] \\ & \doteq \mathcal{J}_{ij}^1 \Delta_j + \mathcal{J}_{ij}^2 \Delta_i \end{aligned} \tag{53}$$

and

$$\begin{aligned} & \frac{\partial \mathbf{C}_{\mathcal{R}}}{\partial \mathcal{A}_{nml}} \Big|_{i,j} \\ &= b_{ij} \mathbf{u}_{i\mathcal{R}}^\top \mathbf{v}_j (\mathbf{J}_1^{-1} - (\mathbf{u}_{i\mathcal{R}}^\top \mathbf{J}_1^{-1}) \mathbf{u}_{i\mathcal{R}})^\top \mathbf{v}_j \Delta_i \\ & \doteq \mathcal{Z}_{ij} \Delta_i, \end{aligned} \tag{54}$$

where

$$\begin{aligned} a_{ij} &= \frac{\beta}{(2\pi \det(\Sigma_{i\mathcal{R}} + \Sigma_{j\mathcal{R}}))^{3/2}}, \\ b_{ij} &= \frac{\beta}{(2\pi \det(\Sigma_{i\mathcal{R}} + \Gamma_{j\mathcal{R}}))^{3/2}}. \end{aligned}$$

Finally we factor out basis functions and their derivatives in Eq. 45 as follows.

$$\begin{aligned} & \boldsymbol{\eta}^\top \frac{\partial \mathbf{A}_{\mathcal{R}}}{\partial \mathcal{A}_{nml}} \boldsymbol{\eta} - 2\boldsymbol{\eta}^\top \frac{\partial \mathbf{C}_{\mathcal{R}}}{\partial \mathcal{A}_{nml}} (\boldsymbol{\rho} \circ \gamma) \\ &= \eta_i \left( \frac{\partial \mathbf{A}_{\mathcal{R}}}{\partial \mathcal{A}_{nml}} \right)_{ij} \eta_j - 2\eta_i \left( \frac{\partial \mathbf{C}_{\mathcal{R}}}{\partial \mathcal{A}_{nml}} \right)_{ij} (\boldsymbol{\rho} \circ \gamma)_j \\ &= \eta_i (\mathcal{J}_{ij}^1 \Delta_j + \mathcal{J}_{ij}^2 \Delta_i) \eta_j - 2\eta_i \mathcal{Z}_{ij} (\boldsymbol{\rho} \circ \gamma)_j \Delta_i \\ &= \eta_i [(\mathcal{J}_{ij}^1 u_{j\mathcal{R}1} + \mathcal{J}_{ij}^2 u_{i\mathcal{R}1}) \eta_j - 2\mathcal{Z}_{ij} (\boldsymbol{\rho} \circ \gamma)_{ju_{i\mathcal{R}1}}] \frac{\partial \Phi_{U_{nml}}}{\partial u} \\ & \quad + \eta_i [(\mathcal{J}_{ij}^1 u_{j\mathcal{R}2} + \mathcal{J}_{ij}^2 u_{i\mathcal{R}2}) \eta_j - 2\mathcal{Z}_{ij} (\boldsymbol{\rho} \circ \gamma)_{ju_{i\mathcal{R}2}}] \frac{\partial \Phi_{U_{nml}}}{\partial v} \\ & \quad + \eta_i [(\mathcal{J}_{ij}^1 u_{j\mathcal{R}3} + \mathcal{J}_{ij}^2 u_{i\mathcal{R}3}) \eta_j - 2\mathcal{Z}_{ij} (\boldsymbol{\rho} \circ \gamma)_{ju_{i\mathcal{R}3}}] \frac{\partial \Phi_{U_{nml}}}{\partial w} \end{aligned} \tag{55}$$

$$\begin{aligned} & 2(\boldsymbol{\rho} \circ \gamma)^\top \mathbf{B} \frac{\partial (\boldsymbol{\rho} \circ \gamma)}{\partial \mathcal{A}_{nml}} - 2\boldsymbol{\eta}^\top \mathbf{C}_{\mathcal{R}} \frac{\partial (\boldsymbol{\rho} \circ \gamma)}{\partial \mathcal{A}_{nml}} \\ &= 2((\boldsymbol{\rho} \circ \gamma)^\top \mathbf{B} - \boldsymbol{\eta}^\top \mathbf{C}_{\mathcal{R}}) \frac{\partial \boldsymbol{\rho}}{\partial \mathbf{u}} \Big|_{\mathbf{u}+\mathbf{U}} \Phi_{U_{nml}} \end{aligned} \tag{56}$$

## Appendix 2

In this section, we show how to evaluate Eqs. 15 and 16. Denote  $J_\gamma$  the determinant of the Jacobian,  $\mathbf{J}_\gamma$  defined in Eq. 7. Its derivative w.r.t.  $\mathcal{A}_{nml}$  defined in Eq. 12 can be written as

$$\begin{aligned} \frac{\partial}{\partial \mathcal{A}_{nml}} J_{\gamma} &= (1 + V_v + W_w + V_v W_w - V_w W_v) \frac{\partial \Phi_{U_{nml}}}{\partial u} \\ &+ (V + w W + u - V_u W_w - V_u) \frac{\partial \Phi_{U_{nml}}}{\partial v} \\ &+ (V_u W_v - V_v W_u - W_u) \frac{\partial \Phi_{U_{nml}}}{\partial w} \end{aligned} \quad (57)$$

Given the derivative of  $J_{\gamma}$ , evaluations of Eqs. 15 and 16 is straightforward:

$$\begin{aligned} \frac{\partial}{\partial \mathcal{A}_{nml}} \sqrt{\kappa_2(\Omega_2 \circ \gamma)} J_{\gamma} \\ = \frac{1}{2\sqrt{\kappa_2}} \frac{\partial \kappa_2}{\partial u} \Big|_{u+U} \Phi_{U_{nml}} J_{\gamma} + \sqrt{\kappa_2} \frac{\partial J_{\gamma}}{\partial \mathcal{A}_{nml}}, \end{aligned} \quad (58)$$

and

$$\begin{aligned} \frac{\partial}{\partial \mathcal{A}_{nml}} (J_{\gamma} - 1) \log(J_{\gamma}) \\ = \left[ \log(J_{\gamma}) + 1 - \frac{1}{J_{\gamma}} \right] \frac{\partial}{\partial \mathcal{A}_{nml}} J_{\gamma}. \end{aligned} \quad (59)$$

## References

- Alexander, D. C., Pierpaoli, C., Basser, P. J., & Gee, J. C. (2001). Spatial transformations of diffusion tensor magnetic resonance images. *IEEE Transactions on Medical Imaging*, 20(11), 1131–1139.
- Ashburner, J., & Friston, K. J. (1999). Nonlinear spatial normalization using basis functions. *Human Brain Mapping*, 7, 254–266.
- Baker, S., Scharstein, D., Lewis, J. P., Roth, S., Black, M., & Szeliski, R. (2011). A database and evaluation methodology for optical flow. *International Journal of Computer Vision*, 92, 1–31.
- Barmpoutis, A., Vemuri, B. C., Shepherd, T. M., & Forder, J. R. (2007). Tensor splines for interpolation and approximation of DT-MRI with applications to segmentation of isolated rat hippocampi. *IEEE Transaction on Medical Imaging*, 26(11), 1537–1546.
- Bates, D. M., Lindstrom, M. J., Wahba, G., & Yandell, B. S. (1987). GCVPACK-Routines for generalized cross validation. *Communications in Statistics—Simulation and Computation*, 16(1), 263–297.
- Beg, M. F., Miller, M. I., Trounev, A., & Younes, L. (2005). Computing large deformation metric mappings via geodesic flows of diffeomorphisms. *International Journal of Computer Vision*, 61(2), 139–157.
- Cachier, P., & Rey, D. (2000). Symmetrization of the non-rigid registration problem using inversion-invariant energies: Application to multiple sclerosis. *International conference on medical image computing and computer assisted intervention, MICCAI* (pp. 472–481).
- Cachier, P., Bardinet, E., Mormont, D., Pennec, X., & Ayache, N. (2003). Iconic feature based nonrigid registration: The PASHA algorithm. *Computer Vision and Image Understanding*, 89(2–3), 272–298.
- Cao, Y., Miller, M.I., Mori, S., Winslow, R.L., & Younes, L. (2006). Diffeomorphic matching of diffusion tensor images, *Proceedings CVPR* (pp. 17–22).
- Chen, T., Rangarajan, A., & Vemuri, B. C. (2010). CAVIAR: Classification via aggregated regression and its application in classifying the OASIS brain database. *IEEE international symposium on biomedical imaging* (pp. 1337–1340).
- Cheng, G., Vemuri, B.C., Carney, P.R., & Marcei, T.H. (2009). Non-rigid registration of high angular diffusion images represented by gaussian mixture fields. *International conference on medical image computing and computer assisted intervention, MICCAI* (1) (pp. 190–197).
- Christensen, G. E., Rabbitt, R. D., & Miller, M. I. (1996). Deformable templates using large deformation kinematics. *IEEE Transactions on Image Processing*, 5(10), 1435–1447.
- Christensen, G. E., & Johnson, H. J. (2001). Consistent image registration. *IEEE Transactions on Medical Imaging*, 20(7), 568–582.
- Christensen, G. E., & Johnson, H. J. (2003). Invertibility and transitivity analysis for non-rigid image registration. *Journal of Electronic Imaging*, 12(1), 106–117.
- Coifman, R. R., Kafon, S., Lee, A. B., Maggioni, M., Nadler, B., Warner, F., et al. (2005). Geometric diffusions as a tool for harmonic analysis and structure definition of data: Diffusion maps. *Proceedings of the National Academy Science*, 102(21), 7426–7432.
- Coifman, R. R., & Lafon, S. (2006). Diffusion maps. *Applied and Computational Harmonic Analysis*, 21, 5–30.
- DoCarmo, M. P. (1992). *Riemannian geometry*. Boston: Birkhauser.
- Gur, Y., & Sochen, N. (2009). *Visualization and processing of tensor fields: advances and perspectives* (pp. 325–340)., Coordinate-based diffusion over the space of symmetric positive-definite matrices Berlin: Springer.
- Jian, B., Vemuri, B. C., Ozarslan, E., Carney, P. R., & Mareci, T. H. (2007). A novel tensor distribution model for the diffusion-weighted MR signal. *NeuroImage*, 37, 164–176.
- Jian, B., & Vemuri, B. C. (2007). A unified computational framework for deconvolution to reconstruct multiple fibers from diffusion weighted MRI. *IEEE Transactions on Medical Imaging*, 26(11), 1464–1471.
- Johnson, H. J., & Christensen, G. E. (2002). Consistent landmark and intensity-based image registration. *IEEE Transactions on Medical Imaging*, 21(5), 450–461.
- Joshi, S., Davis, B., Jomier, M., & Gerig, G. (2004). Unbiased diffeomorphic atlas construction for computational anatomy. *NeuroImage*, 23, 151–160.
- Kimmel, R., & Sochen N.A. (1999). *Geometric-variational approach for color image enhancement and segmentation*, Scale-Space (pp. 294–305).
- Kimmel, R., Malladi, R., & Sochen, N. A. (2000). Images as embedded maps and minimal surfaces: movies, color, texture, and volumetric medical images. *International Journal of Computer Vision*, 39(2), 111–129.
- Koenderink, J., & van Doorn, A. J. (2002). Image processing done right. *Proceedings of ECCV*, 1, (pp. 158–172).
- Kroon, D.J., & Slump, K. (2009). MRI modality transformation in Demon registration. *IEEE international symposium on biomedical imaging* (pp. 963–966).
- Kurtek, S., Klassen, E., Ding, Z., Srivastava, A. (2010). *A novel Riemannian framework for shape analysis of 3D objects*, *Proceedings of CVPR*, (pp. 1625–1632).
- Kurtek, S., Klassen, E., Ding, Z., Avison, M. J., & Srivastava, A. (2011). Parameterization-invariant shape statistics and probabilistic classification of anatomical surfaces. *IEEE Transactions on Medical Imaging*, 30(3), 49–858.
- Litke, N., Droske, M., Rumpf, M., & P. Schröder. (2005). An image processing approach to surface matching, *symposium on geometry processing*, (pp. 207–216).
- Marcus, D. S., Wang, T. H., Parker, J., Csernansky, J. G., Moris, J. C., & Buckner, R. L. (2007). Open access series of imaging studies (OASIS): Cross-sectional MRI data in young, middle aged, non-demented, and demented older adults. *Journal of Cognitive Neuroscience*, 19, 1498–1507.

- Moakher, M. (2006). A differential geometric approach to the geometric mean of symmetric positive-definite matrices. *SIAM Journal on Matrix Analysis and Applications*, 26(3), 735–747.
- Seo, D., & Vemuri, B. (2009). *Complex diffusion on scalar and vector valued image graphs*, *Proceedings of EMMCVPR* (pp. 98–111).
- Sochen, N. A., Kimmel, R., & Malladi, R. (1998). A general framework for low level vision. *IEEE Transactions on Image Processing*, 7(3), 310–318.
- Tagare, H. D., Groisser, D., & Skrinjar, O. (2009). Symmetric non-rigid registration: a geometric theory and some numerical techniques. *Journal of Mathematical Imaging and Vision*, 34, 61–88.
- Tuch, D.S. (2002). Diffusion MRI of complex tissue structure, PhD thesis, MIT.
- Vercauteren, T., Pennec, X., Perchant, A., & Ayache, N. (2007). Non-parametric diffeomorphic image registration with the Demons algorithm, *International conference on medical image computing and computer assisted intervention, MICCAI 2*, (pp. 319–326).
- Xie, Y., Vemuri, B.C., & Ho, J. (2010). Statistical analysis of tensor fields. *International conferences on medical image computing and computer assisted intervention, MICCAI 1* (pp. 682–689).
- Yanovsky, I., Thompson, P.M., Osher, S., & Leow, A.D. (2007). Topology preserving Log-unbiased nonlinear image registration: Theory and implementation. *Proceedings of CVPR* (pp. 1–8).
- Zhang, P., Wee, C.-Y., Niethammer, M., Shen, D., & Yap, P.-T. (2013). Large Deformation Image Classification Using Generalized Locality-Constrained Linear Coding. *International conference on medical image computing and computer assisted intervention, MICCAI*.